Global Biogeochemical Cycles

RESEARCH ARTICLE
10.1029/2020GB006922

# Characterizing Methane Emission Hotspots From Thawing Permafrost

**C. D. Elder[1], D. R. Thompson[1], A. K. Thorpe[1], H. A. Chandanpurkar[1,2,3], P. J. Hanke[4], N. Hasson[4], S. R. James[5], B. J. Minsley[5], N. J. Pastick[6], D. Olefeldt[7], K. M. Walter Anthony[4], and C. E. Miller[1]**

[1]Jet Propulsion Laboratory, California Institute of Technology, Pasadena, CA, USA, [2]Global Institute for Water Security, University of Saskatchewan, Saskatoon, SK, Canada, [3]Centre for Earth and Environment, FLAME University, Pune, India, [4]Water and Environmental Research Center, University of Alaska Fairbanks, Fairbanks, AK, USA, [5]Geology, Geophysics, and Geochemistry Science Center, U.S. Geological Survey, Denver, CO, USA, [6]KBR, U.S. Geological Survey, Earth Resources Observation and Science Center, Sioux Falls, SD, USA, [7]Department of Renewable Resources, University of Alberta, Edmonton, AB, Canada

**Key Points:**

- Repeat airborne spectral imaging geolocated a thermokarst methane ($CH_4$) hotspot with ground-validated emissions >10 g $CH_4$ $m^{-2}$ $d^{-1}$
- Hotspot $CH_4$ emissions arose from <1% of our 10 ha thermokarst lake study area but comprised ~40% of the total diffusive emissions
- Ground-based and airborne observations suggest thermokarst hotspots emit roughly 1.1 Tg $CH_4$ $yr^{-1}$ or 4% of pan-Arctic wetland $CH_4$ emissions

**Supporting Information:**

Supporting Information may be found in the online version of this article.

**Correspondence to:**

C. D. Elder,
clayton.d.elder@jpl.nasa.gov

**Citation:**

Elder, C. D., Thompson, D. R., Thorpe, A. K., Chandanpurkar, H. A., Hanke, P. J., Hasson, N., et al. (2021). Characterizing methane emission hotspots from thawing permafrost. *Global Biogeochemical Cycles*, *35*, e2020GB006922. https://doi.org/10.1029/2020GB006922

Received 16 DEC 2020
Accepted 10 NOV 2021



## Abstract

Methane ($CH_4$) emissions from climate-sensitive ecosystems within the northern permafrost region represent a potentially large but highly uncertain source, with current estimates spanning a factor of seven (11–75 Tg $CH_4$ $yr^{-1}$). Accelerating permafrost thaw threatens significant increases in pan-Arctic $CH_4$ emissions, amplifying the permafrost carbon feedback. We used airborne imaging spectroscopy with meter-scale spatial resolution and broad coverage to identify a previously undiscovered $CH_4$ emission hotspot adjacent to a thermokarst lake in interior Alaska. Hotspot emissions were confined to <1% of the 10 ha lake study area. Ground-based chamber measurements confirmed average daily fluxes from the hotspot of 1,170 mg $CH_4$ $m^{-2}$ $d^{-1}$, with extreme daily maxima up to 24,200 mg $CH_4$ $m^{-2}$ $d^{-1}$. Ground-based geophysical measurements revealed thawed permafrost directly beneath the $CH_4$ hotspot, extending to a depth of ~15 m, indicating that the intense $CH_4$ emissions likely originated from recently thawed permafrost. Hotspot emissions accounted for ~40% of total diffusive $CH_4$ emissions from the lake study site. Combining study site findings with hotspot statistics from our 70,000 $km^2$ airborne survey across Alaska and northwestern Canada, we estimate that pan-Arctic terrestrial thermokarst hotspots currently emit 1.1 (0.1–5.2) Tg $CH_4$ $yr^{-1}$, or roughly 4% of the annual pan-Arctic wetland budget from just 0.01% of the northern permafrost land area. Our results suggest that significant proportions of pan-Arctic $CH_4$ emissions originate from disproportionately small areas of previously undetermined thermokarst emissions hotspots, and that pan-Arctic $CH_4$ emissions may increase non-linearly as thermokarst processes increase under a warming climate.

## Plain Language Summary

We conducted high-resolution airborne surveys of near-surface methane ($CH_4$, a powerful greenhouse gas) anomalies in permafrost ecosystems in Alaska and northwestern Canada as part of NASA's Arctic Boreal Vulnerability Experiment (ABoVE). These measurements provided fine-scale resolution for the remote detection of $CH_4$ emission hotspots from natural Arctic environments. Repeated flights over Big Trail Lake near Fairbanks, AK revealed a previously undiscovered $CH_4$ hotspot at this intensive study site. Ground-based measurements confirmed extremely high surface-to-atmosphere emissions at this location, on the shore of a permafrost-thaw pond that formed after 1963. Geophysical surveys confirmed the presence of thawed permafrost underneath the hotspot, extending to a depth ~15 m. We hypothesize that recent permafrost thaw and subsidence made soils with highly decomposable organic carbon available for microbial metabolism, conversion into $CH_4$, and enhanced emission to the atmosphere. Extrapolating our observed hotspot fluxes across the pan-Arctic, we estimate that thermokarst $CH_4$ hotspots constitute less than 0.01% of the pan-Arctic land area, but contribute roughly 4% of annual pan-Arctic wetland emissions. We further hypothesize that Arctic $CH_4$ emissions may grow significantly in the future with anticipated increases in thermokarst across the permafrost landscape.

## 1. Introduction

Pronounced warming of the northern high-latitudes is causing rapid permafrost thawing and subsequent collapse of ground surfaces (thermokarst) (Farquharson et al., 2019; Lewkowicz & Way, 2019), threatening the stability of the 1,300–1,600 Pg permafrost carbon (C) reservoir (Schuur et al., 2015). The effect of widespread thermokarst

and/or abrupt thaw on pan-Arctic greenhouse gas (GHG) emissions is poorly understood despite its potential impact to global climate. Turetsky et al. (2020) estimate that abrupt permafrost thaw processes may add an additional 40 ± 10% to net C emission or 0.30 W $m^{-2}$ net radiative forcing beyond that expected from gradual deepening of the seasonally thawed active layer through year 2300. Uncertainties in future anthropogenic C emissions, along with uncertainties inherent to modeling heterogeneous Arctic landscapes, result in broad disagreement on both the sign and magnitude of forecasted net C exchange from permafrost regions through the 23rd century (McGuire et al., 2018). This emphasizes the need to improve our observational capabilities of the Arctic C cycle, especially for $CH_4$ emissions due to their 25–30 times greater potency as a GHG compared to carbon dioxide ($CO_2$) on a 100-year timescale. This potency means $CH_4$ emissions from abruptly thawing permafrost may constitute 50% of the total future radiative forcing from permafrost emissions, despite emissions being four times lower than $CO_2$ (Turetsky et al., 2020). Extreme spatiotemporal variability of $CH_4$ emissions from heterogenous permafrost environments further compounds the uncertainty related to forecasting the permafrost C feedback in a rapidly warming Arctic.

Growing evidence links high $CH_4$ emissions to intense areas of abrupt permafrost thaw and mobilization of highly labile and ancient permafrost organic carbon (Serikova et al., 2019; Walter Anthony et al., 2016). However, the extent and impact of abrupt thaw and/or thermokarst emissions on the pan-Arctic $CH_4$ budget is unclear. This is especially so since young/contemporary carbon sources dominate whole-lake and diffusive wetland GHG emissions in some high latitude studies (Cooper et al., 2017; Dean et al., 2020; Elder et al., 2018), and some evidence suggests that Arctic $CH_4$ emissions have likely not increased significantly over the last 40 years (Sweeney et al., 2016). Estimating annual pan-Arctic $CH_4$ emissions is challenging due to a paucity of in situ observations and detailed geospatial datasets (e.g., wetland type and distribution, thermokarst landforms, soil moisture, etc.) needed to accurately scale emission patterns across heterogeneous permafrost landscapes (Bloom et al., 2017; Morel et al., 2019). A key contributor to this uncertainty is the propensity of large proportions of total emissions to originate from tiny fractions of the landscape, further challenging field research and modeling efforts (Turetsky et al., 2020). As a result, Arctic $CH_4$ emission estimates span a factor of seven across process-based and inversion models (11–75 Tg $CH_4$ $yr^{-1}$) and flux upscaling (21–54 Tg $CH_4$ $yr^{-1}$) (McGuire et al., 2012; Peltola et al., 2019). Constraining budget estimates and model behavior will require a combination of expanded process-oriented field observations, determination of key spatial metrics, and mechanistic insights derived from complementary high-resolution remote sensing (Elder, Thompson, et al., 2020).

Here, we combined metrics from a synoptic-scale airborne $CH_4$ hotspot survey of Alaska and western Canada (Elder, Thompson, et al., 2020) with new ground-based and airborne remote sensing observations of permafrost structure and extreme $CH_4$ emissions at a thermokarst lake, 8 km north of Fairbanks, Alaska. This allowed us to estimate $CH_4$ fluxes attributable to active thermokarst morphology across the northern permafrost domain. In this work, we utilized an airborne $CH_4$ hotspot data set, unprecedented in spatial resolution and coverage, to investigate and estimate the influence of thermokarst on $CH_4$ hotspot emissions from plot scales to pan-Arctic scales. Where Elder, Thompson, et al. (2020) took a broad-scale statistical approach to investigate emergent hotspot patterns, this study investigated the mechanisms behind hotspot emissions, quantifying hotspot fluxes, apportioning them in the context of our thermokarst lake study environment, and extrapolating to pan-Arctic scales. Our study demonstrated the ability to detect anomalous $CH_4$ fluxes at high-resolution across large spatial domains, which is critical for informing ground-based study and for accurate spatial upscaling. Our findings represent a unique observation-based approach to estimating contemporary pan-Arctic terrestrial thermokarst $CH_4$ emissions, which are expected to dramatically increase within the next century.

## 2. Methods

### 2.1. $CH_4$ Patterns at High Spatial Resolution Across Broad Scales

NASA's Arctic Boreal Vulnerability Experiment (ABoVE) surveyed over 70,000 $km^2$ of Alaska and northwestern Canada with the Next Generation Airborne Visible/Infrared Imaging Spectrometer (AVIRIS-NG) during the summers of 2017, 2018, and 2019 (C. E. Miller et al., 2019). AVIRIS-NG was installed on a KingAir B-200 (Dynamic Aviation, tail number N53W) which flew at altitudes from 2 to 6 km above ground level (AGL), providing ground sampling distances (pixel dimensions) of 2–6 m.

AVIRIS-NG maps $CH_4$ concentration hotspots with meter-scale spatial resolution by measuring shortwave infrared (SWIR) $CH_4$ absorption features present in surface-reflected solar radiation. The remote measurement used a matched filter approach presented in Thompson et al. (2015), and deployed in multiple subsequent campaigns (Cusworth et al., 2020; Duren et al., 2019; Elder, Thompson, et al., 2020; Frankenberg et al., 2016; Thorpe et al., 2020). A complete description appears in the Methods in Supporting Information S1. The remote mapping process produced maps quantifying the $CH_4$ absorption above background levels in between the sensor and the surface in integrated concentration path-length units, ppm × m. Subsequent analyses of these $CH_4$ enhancement images identified "hotspots," which we operationally defined as enhanced pixels with a minimum of 2,500–3,000 ppm × m excess $CH_4$ above background concentrations. This threshold typically represented a minimum signal-to-noise ratio of three to four. In lower altitude ABoVE surveys (<3 km AGL), pixels are smaller and AVIRIS-NG was more sensitive to column $CH_4$ absorption, however scene heterogeneity often inflated spectrometer noise. While AVIRIS-NG can observe $CH_4$ over open water in sun glint conditions (Thorpe et al., 2013, 2014), flight lines in this study were not planned to optimize glint. Thus, our $CH_4$ measurements were limited to terrestrial surfaces leading up to the water's edge and the hotspots discussed here should be considered terrestrial or littoral when emergent plants create a SWIR-reflective canopy over standing water.

### 2.2. Remote Detection of Hotspots at Big Trail Lake

During the 2018 and 2019 ABoVE airborne campaigns (AAC), AVIRIS-NG targeted Big Trail Lake (BTL; 64.91940° and −147.82222°) and its adjacent thermokarst pond (informally named "Eastside Pond" hereafter). These sites benefited from ongoing ground validation of $CH_4$ emissions monitoring (Elder, Thompson, et al., 2020), and their location along the flight approach to Fairbanks International Airport, the regional base of operations for AVIRIS-NG. The latter allowed for 17 successful overflights of BTL at multiple survey altitudes and sun angles, enabling repeated hotspot analysis. See Methods in Supporting Information S1 for a description of the $CH_4$ retrieval process.

Elder, Thompson, et al. (2020) intensively surveyed $CH_4$ fluxes with chambers at 169 locations within the main lake body and on radial transects in the nearshore environment of BTL in July of 2018. Despite the intensive ground-based survey, hotspots were not geolocated until raw AVIRIS-NG data was processed following the 2018 field campaign, revealing a persistent $CH_4$ hotspot on the eastern margin of the Eastside Pond. During the 2019 field campaign, ground-based flux surveys were repeated with some additional methods designed to validate hotspot fluxes (detailed below and in the Methods in Supporting Information S1). In 2019, we also enacted a fast data transfer protocol to enable overnight processing of 2019 AVIRIS-NG output data and rapid production of $CH_4$ hotspot maps. These maps again revealed a hotspot in the same location as in 2018 at the Eastside Pond (Figure 1). Overnight maps were then used to guide in situ validation surveys at BTL within 24–48 hr of the 2019 AVIRIS-NG overflights.

### 2.3. Site Description of Big Trail Lake

BTL is an active thermokarst lake recently formed atop degrading ice-rich Yedoma soils on public lands in the Goldstream Creek watershed of interior Alaska. Airborne photographic records indicate that BTL formed from a fen wetland sometime between 1949 and 1967 and has since expanded to 4.15 ha (Walter Anthony et al., 2018). Multiple rivulet streams draining surrounding fens, including a remnant flow path of Goldstream Creek, feed the Eastside Pond. In some of the inlet streams, the water flows ephemerally. Water leaves the Eastside Pond through a 10-m-wide channel feeding into the east side of BTL. A narrow outlet drains BTL's main lake body from the southwest corner. The shallow portions of the main body of BTL support communities of macrophytes including abundant *Potamogeton*. The shorelines of BTL and Eastside Pond have abundant hydrophytic vegetation communities (i.e., genus: *Typha*, *Carex*, *Equisetum*, *Juncus*, etc.), many with aerenchyma that can serve as a conduit for $CH_4$ to escape to the atmosphere (Ström et al., 2003).

A persistent remotely sensed $CH_4$ hotspot was detected along the eastern shoreline of the Eastside Pond (Figure 1). Although not unique at BTL, this shoreline is characterized by a rapid transition from non-emergent and emergent littoral vegetation to upland vegetation species along steep erosional banks (Figure S1 in Supporting Information S1). Two to three rivulet streams, which drain the small fen ~70 m to the east, converge at the location of the $CH_4$ hotspot along the eastern margin of the Eastside Pond and likely contribute to enhanced thermokarst

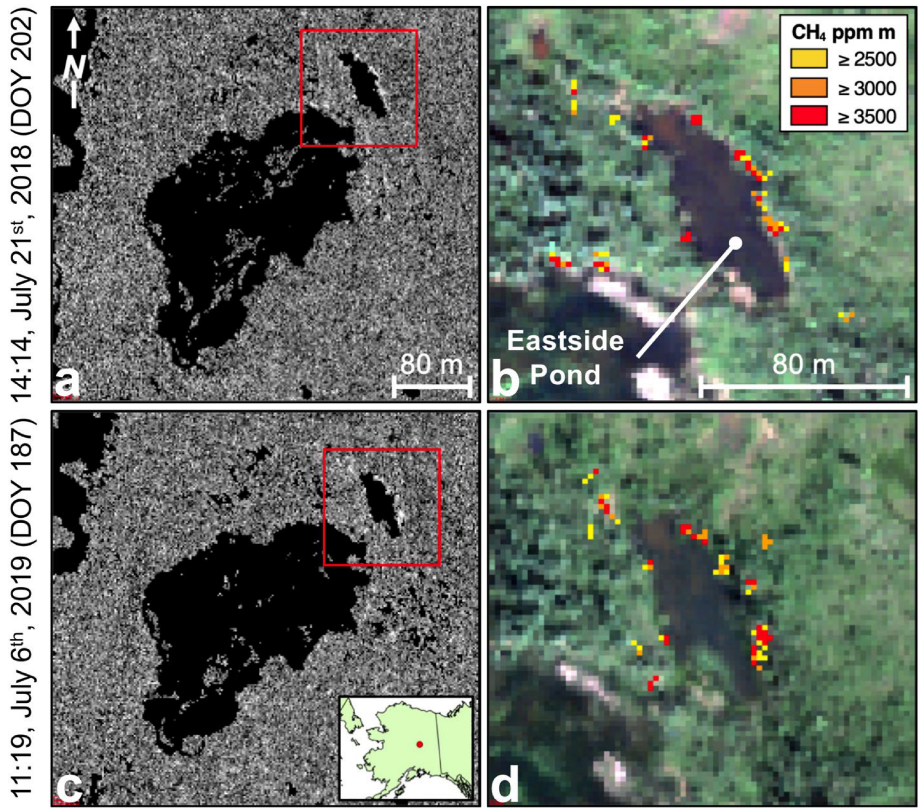


**Figure 1.** Next Generation Airborne Visible/Infrared Imaging Spectrometer remote detection of $CH_4$ hotspots at the Eastside Pond of Big Trail Lake (64.91932°N, −147.82200°W) in July 2018 (a) and (b) and July 2019 (c) and (d). 2019 image was taken 2 hr before the ground-based survey shown in Figure 2. Greyscale panels (a) and (c) show surface-controlled matched filter spectrometer output for column $CH_4$ enhancement. Panels (b) and (d) show RGB channels overlaid with spectrometer output for spatially filtered $CH_4$ hotspots. Red outlines in the left images denote the extent of the RGB images. Local time of imagery is shown (Alaska Daylight Time).

at the site. The Eastside Pond initially formed sometime between 1967 and 1985 (Walter Anthony et al., 2018). We estimate from aerial photography in Walter Anthony et al. (2018) that the Eastside Pond has expanded by 0.5–1 m $yr^{-1}$ since formation. Its formation was likely influenced to some extent by the development of an unpaved, single-lane access road which was built in the mid twentieth century. Despite the road being un-maintained and impassable for many years due to flowing water and seasonal flooding, it still serves as a recreational path to cross country skiers and mushers when the Eastside Pond freezes in winter. Multiple other thermokarst ponds occur along the old ~1 km road, however it is unknown to what extent the road's presence affects contemporary thermokarst or $CH_4$ emissions in the thermokarst-rich Goldstream Valley.

### 2.4. Ground-Based Enhancement and Flux Surveys

We performed a ground-based $CH_4$ enhancement survey on 6 July 2019 between 13:25 and 17:15 Alaska Daylight Time (UTC-8). This survey confirmed hotspots detected at the Eastside Pond by AVIRIS-NG on the previous day and approximately 2 hr prior during an additional overflight on the morning of the sixth (Figure 1). During the ground-based enhancement survey, atmospheric $CH_4$ concentrations were measured on foot at 1 Hz with a Los Gatos Ultra-Portable Greenhouse Gas Analyzer (UGGA) (ABB INC., 85 Quebec City, CA). Measurements were made at approximately 0.5 m AGL while walking along a ~10 cm $s^{-1}$ snaking transect starting in the southwest and working northeast of the hotspot region (Figure 2). The inlet to the UGGA was fitted to the lid of a 5-gallon bucket with the bottom removed to minimize interference from non-local sources and held at arm's length in front of the surveyor. Wooden planks, which were placed at least 1 hr before measurement, were used as footpaths in sensitive environments to minimize disturbance. The geolocation accuracy of mapped $CH_4$ concentrations is estimated to be ±5 m, with uncertainties dominated by lags in handheld GPS updates during the walking survey.

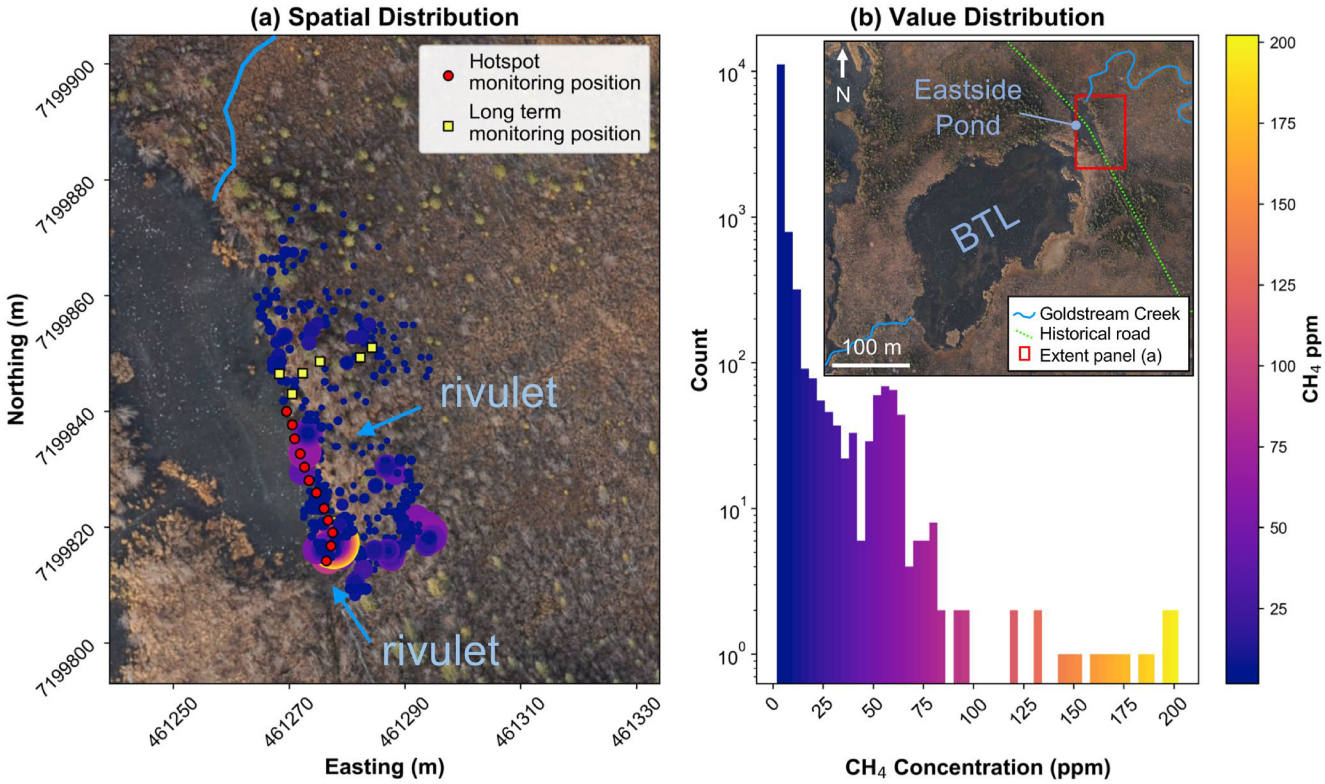


**Figure 2.** Ground-based $CH_4$ enhancement survey on 6 July 2019 between 13:25 and 17:15 local time. Color scale in panels (a) and (b) correspond to $CH_4$ concentrations measured in ppm in air at ~0.5 m above ground level along a 10 cm/s snaking transect that began in the SW and ended in the NE in panel (a) (see color bar for $CH_4$ scale). Gas concentration data was recorded at 1 Hz. GPS position was updated every 30 s. The size of the points in panel (a) are also scaled to their corresponding $CH_4$ ppm values. Individual points in panel (a) represent multiple gas concentration measurements but appear stacked due to lagged GPS updates. As a result, concentration data is accurate to ±5 m. Red circles represent seasonal hotspot flux monitoring locations, whereas yellow squares represent long term flux monitoring with permanent chamber-collars (flux data not shown here).

In addition to measuring ground-level $CH_4$ enhancements in the free air, hotspot flux monitoring measurements at the Eastside Pond $CH_4$ hotspot were also implemented in July 2019 to further validate airborne detections. Hotspot monitoring chambers, constructed from plastic five-gallon buckets with bottoms removed and resealable air-tight lids (Gamma Seal Lid, Encore Plastics, Sandusky, OH, USA) (Figure S2 in Supporting Information S1), were installed at hotspot flux monitoring locations (Figure 2). All diffusive fluxes, including non-hotspot measurements (described below), were calculated from the ideal gas law using chamber volume and temperature, and atmospheric pressure measured via a LI-COR LI7700 (LI-COR Inc., Lincoln, Nebraska, USA) operating mid-BTL. The slope of linear $CH_4$ concentration change ($R^2 > 0.985$ correlation to linear least squares fit) for a minimum of 45 s (45 observations) and a maximum of 210 s ($45 < n > 210$) was used to determine mass change within the chambers. Chamber observation periods were ≤5 min and observations within the first 3.5 min of chamber placement were prioritized. Any observations with non-linear concentration change ($R^2$ of linear fit <0.985), no linear sections ≥45 s, or with stepwise concentration increases (interpreted as ebullition) were omitted to ensure that the reported measurements represent purely diffusive fluxes. These strict protocols eliminated any disturbance caused by placing the chamber, which we assume would manifest as non-linear $CH_4$ concentration change. See the Methods in Supporting Information S1 for more details regarding the processing of raw chamber data and data quality protocols.

Bucket chambers were installed such that 2–5 cm of the open bottom was submerged in saturated sediments to create a hermetic seal. These hotspot monitoring positions ($n = 12$) were equally spaced 3–4 m apart on sparsely vegetated or bare, saturated surfaces along the southeastern shoreline of the Eastside Pond where the water table was nearest to the surface, or where we expected the highest diffusive fluxes. Buckets were left in place, sans lid, for at least 24 hr before fluxes were measured and remained in place until removal just before seasonal freeze up. Plant mediated $CH_4$ emission potentially contributed to total observed flux in cases where buckets included

sparse emergent vegetation and flux was linear. A singular bucket was placed on the snow surface at the hotspot location to observe fluxes on 14 December 2019. The chamber volume was corrected for snow density inside the chamber for this measurement. During all flux measurements, lids fitted with ¼" PVC valves were gently screwed into the top of each bucket, creating an air-tight closed chamber to recirculate air through the UGGA. Lids were removed after each measurement. All hotspot fluxes reported here were measured on 5 days in between 7 July 2019 and 17 September 2019, and on 14 December 2019, resulting in 66 total observations from the Eastside Pond hotspot region. Hotspot fluxes were not measured at night; therefore, we assume our daytime measurements capture the diel variability of $CH_4$ hotspot emissions. This may represent a source of error in our extrapolations, though this potential effect was not quantified. All fluxes were measured between the hours of 09:35–17:32 local time.

Non-hotspot $CH_4$ fluxes were monitored from various surfaces at BTL via repeat chamber-flux measurements along five shore-to-forest transects since summer 2018 (Elder, Hanke, et al., 2020), following methods described in Elder, Thompson, et al. (2020). Starting in July 2019, fluxes were also measured as in Elder, Thompson, et al. (2020), except that instead of placing chambers directly on the surface, permanent aluminum chamber-collars were installed to 3–5 cm depth at long-term flux monitoring locations both near the hotspot and other locations of BTL. Aluminum collars were in place for a minimum of 1 week before flux measurements were made. A removable flotation system constructed of pipe insulation was attached to the chamber for measurements over open water. As described in Elder, Thompson, et al. (2020), a larger transparent chamber was used at all non-hotspot locations and was designed to enclose vegetation up to ~1.5 m in height. Therefore, like the hotspot monitoring, these observations also included potential plant-mediated fluxes when vegetation was present in the chamber and fluxes were linear. Thus, fluxes reported herein should be considered as inclusive of linear plant-mediated emissions but exclusive of ebullitive emissions. Since ebullition was not determined from any of our chamber observations, our estimates are conservative with respect to total emissions.

### 2.5. Relating Hotspot $CH_4$ Fluxes to AVIRIS-NG Observations

Previous controlled release experiments determined the lower limit of AVIRIS-NG $CH_4$ flux detectability to be ~2 kg $CH_4$ $hr^{-1}$ from point sources (Thorpe et al., 2016). While this flux rate is much higher than common $CH_4$ emission rates from northern wetlands, we expect AVIRIS-NG to be sensitive to significantly smaller fluxes when air stagnation and the size of typical ecological hotspots are taken into account. We developed a simple diffusion and advection plume model (Equation S3 in Supporting Information S1), to link ground-based observations with AVIRIS-NG observations and quantify the conditions necessary for AVIRIS-NG hotspot detection. We simulated diffusion rates based on typical in situ observations in an artificial 10 × 10m hotspot from the Eastside Pond (5 × 5 grid of 2.1 m pixels) to model expected AVIRIS-NG remote observations at various wind-controlled plume turnover rates (proportional to lifetime of $CH_4$ enhancement within AVIRIS-NG detected plumes). See Methods in Supporting Information S1 for a more detailed explanation. The maximum $CH_4$ enhancement observed at ground level (202 ppm $CH_4$) was then used in the hotspot simulation model to determine the effective wind speed and plume turnover time necessary to accumulate this $CH_4$ concentration given the prescribed hotspot fluxes.

### 2.6. ERT and NMR Geophysical Observations

In early September 2019, we conducted ground-based electrical resistivity tomography (ERT) geophysical surveys perpendicular to the north, east, and south shorelines of BTL, and collected borehole nuclear magnetic resonance (NMR) data adjacent to the north and east survey lines (James et al., 2020). Here, we focus on the eastern survey which transects the persistent Eastside Pond $CH_4$ hotspot. ERT images subsurface permafrost structure along 2D profiles to depths of 40–50 m by measuring spatial variations in electrical resistivity along a line of electrodes planted in the ground surface. Electrical resistivity is highly sensitive to the presence of liquid water, so thawed or wet zones exhibit vastly different values compared to dry or frozen soils (Briggs et al., 2017; Lewkowicz et al., 2016; Minsley et al., 2015, 2016). NMR was used to observe total liquid water content and relative pore size distributions at 12.5 cm depth intervals from the surface to a depth of 2.1 m. NMR data were measured at a single location adjacent to the east ERT survey line, just inland on the eastern margin of the Eastside Pond. See Methods in Supporting Information S1 for a more detailed description of the ERT and NMR observation methods.

### 2.7. AVIRIS-NG Surface Classification for BTL $CH_4$ Flux Upscaling

The fraction of the $CH_4$ flux contributed by the Eastside Pond hotspot to the total $CH_4$ flux from all other surfaces in the BTL environment remained a critical question. To address it, we classified surfaces at BTL and its surrounding nearshore environment by analyzing a ~300 × 300 m sub-scene of AVIRIS-NG 426-band reflectance imagery collected on 5 July 2019. From this sub-scene, a spectral library of prominent surface classes was developed based on a combination of expert-knowledge sub-sampling of BTL imagery and ground-based spectrometer surveys (ASD FieldSpec 4, ASD Products, Cambridge, UK) collected in July of 2019. Spectral endmembers were used in an iterative multiple endmember spectral mixture analysis (MESMA) (Roberts et al., 1998) to classify nine surfaces within a 50 m perimeter surrounding the open water of BTL and the Eastside Pond. Spectral analysis also included open water surfaces. The 50 m terrestrial perimeter represents the boundary at which ground-based $CH_4$ flux observations extended from the shoreline. The resulting surface classification map was used to upscale $CH_4$ fluxes using chamber observations recorded in summer 2018 and 2019 from corresponding surface types. Surface classifications included: open water, surface macrophytes (mostly *Potamogeton*), bare sediment, *Typha*, mixed wet grasses, dry grass + broadleaf, *Equisetum* dominant, mixed spruce, and senesced vegetation.

Previously published, surface-specific fluxes observed from BTL in 2018 ($n = 169$) (Elder, Hanke, et al., 2020) were combined with new fluxes observed in 2019 ($n = 158$) to derive median growing-season $CH_4$ fluxes for each surface type at BTL. Since flux distributions were typically positively skewed, median fluxes for each surface were used. These values were then multiplied by the area of each surface type within the domain to estimate total daily diffusive flux from BTL and its nearshore environment. Median flux from mixed wet grasses was applied to unclassified surfaces (<1% of total surface area) and senesced vegetation surfaces (3.1% of total surface area) since chamber flux observations did not disambiguate these surface types, and because they typically occurred within the mixed wet grass category at BTL. The mean of daily maximum flux rate (from in situ closed chamber measurements) was used instead of the median for AVIRIS-NG-identified $CH_4$ hotspot surfaces. This was due to the variable nature of extreme $CH_4$ emission events within the chamber-flux data set and the likely flux detection threshold of AVIRIS-NG as informed by the plume diffusion and advection model (Equation S3 in Supporting Information S1). Diffusive fluxes from the 9 unique surface types, including their upscaled proportion of total study area fluxes are summarized in Table S1 in Supporting Information S1.

### 2.8. Upscaling Thermokarst $CH_4$ Hotspot Emissions to the Pan-Arctic

Airborne mapping of $CH_4$ hotspots across Alaska and western Canada during the 2017, 2018, and 2019 AACs allowed us to characterize $CH_4$ hotspot abundance and distribution over a diverse 70,000 $km^2$ domain well beyond BTL. We assessed hotspot relationships within this domain with respect to thermokarst occurrence, applied our ground-observed $CH_4$ emission rates from BTL, and extrapolated thermokarst $CH_4$ hotspot fluxes across the pan-Arctic. Using two independent approaches, we produced a total of six estimates to bracket the likely range of annual pan-Arctic $CH_4$ emissions from thermokarst hotspots ($E_{HS}$) by manipulating variables in the following equation:

$$E_{HS} = R_{\psi,\phi} \cdot A_{\delta,\beta} \cdot F_{a,b,c} \cdot t \quad (1)$$

where $R$ equaled one of two $CH_4$ hotspot occurrence ratios ($R_\psi$ or $R_\phi$) determined from ABoVE-domain-wide AVIRIS-NG data. $R_\psi$ or $R_\phi$ were then paired with two different upscaling areas ($A_\delta$ or $A_\beta$, respectively). Hotspot occurrence ratios ($R_\psi$ or $R_\phi$) were calculated as the ratio of total hotspot area to the total surveyed terrestrial area in a defined region.

In the first approach, $R_\psi$ equaled the area-weighted mean hotspot ratio from terrestrial surfaces within environments classified by Olefeldt et al. (2016) as having "very high" wetland and/or lake-type thermokarst occurrence in a subset of 52 AVIRIS-NG flight lines from 2017, 2018, and 2019 ($R_\psi = 0.054\%$). The 52-flight-line subset consisted of a ~5,600 $km^2$ surveyed area, representing variable wetlands, lake types, glacial history, and levels of thermokarst occurrence. To test the hypothesis that $R_\psi$ was greater in regions with greater thermokarst occurrence, $R_\psi$ was also determined from five additional flight lines overlapping regions classified as intermediate wetland/lake thermokarst and seven additional flight lines overlapping "low" wetland/lake thermokarst. This resulted in a total of 64 flight lines, representing a ~7,000 $km^2$ subset survey. Hillslope-type thermokarst regions were not considered since they are least likely to collect water and produce the anoxic conditions needed for high

**Table 1**
*Estimating Annual Pan-Arctic $CH_4$ Hotspot Fluxes Attributable to Thermokarst Processes Using Estimates of Mapped Thermokarst, AVIRIS-NG Hotspot Metrics, and Flux Magnitudes Observed on the Ground From a Persistent Hotspot at the Eastside Pond*

| Upscaling area description | Upscaling area ($m^2$) ($A$) | Hotspot occurrence ratio (%) ($R$) | $CH_4$ flux (mg $m^{-2}$ $d^{-1}$) ($F$) | Flux days$^{-yr}$ ($t$) | Pan-arctic hotspot flux (g $CH_4$ $yr^{-1}$) ($E_{HS}$) | % Of total wetland flux >45°N[h] |
|---|---|---|---|---|---|---|
| Very high lake and/or wetland thermokarst occurrence | $1.978 \times 10^{12}$[d] | 0.054[f] | 1,168[a] | 200 | $2.5 \times 10^{11}$ | 0.8 |
| | | | 7,984[b] | | $1.7 \times 10^{12}$ | 5.3 |
| | | | 24,227[c] | | $5.2 \times 10^{12}$ | 16.2 |
| Active lake and wetland thaw features | $1.498 \times 10^{11}$[e] | 0.243[g] | 1,168[a] | 200 | $8.5 \times 10^{10}$ | 0.3 |
| | | | 7,984[b] | | $5.8 \times 10^{11}$ | 1.8 |
| | | | 24,227[c] | | $1.8 \times 10^{12}$ | 5.5 |
| Median | | | | | $1.1 \times 10^{12}$ | 3.6 |

*Note*. Letters in parenthesis correspond to variables in Equation 1.

[a]Mean of BTL hotspot flux data ($F_a$, $n = 66$). [b]Mean of daily maximum BTL hotspot fluxes ($F_b$, $n = 5$). [c]Maximum observed BTL hotspot flux ($F_c$, $n = 1$). [d]Olefeldt et al. (2016) upscaling area ($A_\delta$). [e]Turetsky et al. (2020) upscaling area ($A_\beta$). [f]Area-weighted mean hotspot ratio ($R_\psi$) from terrestrial surfaces in a 7,000 $km^2$ subset of ABoVE survey (see text). [g]Mean hotspot ratio ($R_\phi$) within 45 m of open water bodies in Elder, Thompson, et al. (2020). [h]Annual Pan-Arctic flux of 32 Tg $CH_4$ $yr^{-1}$ from Peltola et al. (2019).

$CH_4$ production. Flight lines were chosen for their observation quality and representativeness. We assume the 7,000 $km^2$ subset of AVIRIS-NG flight lines, which sub-samples the spatial extent of the $6.3 \times 10^6$ $km^2$ ABoVE study domain, was spatially representative of diverse lake and wetland types found throughout the pan-Arctic. $R_\psi$ was then multiplied by $A_\delta$, which represented the area of all high-latitude terrain likely to contain "very high" rates of thermokarst occurrence. Since the AVIRIS-NG $CH_4$ survey only measured land surfaces, we subtracted open water thaw lake area (280,000 $km^2$; Turetsky et al., 2020) from the total pan-Arctic mapped area classified as "very high" in both of the thermokarst lake and/or thermokarst wetland categories in Olefeldt et al. (2016). This produced a pan-Arctic terrestrial upscaling area of $A_\delta = 1{,}978{,}000$ $km^2$. The product of $R_\psi \cdot A_\delta$ represents our estimate total thermokarst $CH_4$ hotspot area in terrestrial pan-Arctic regions of "very high" wetland and/or lake thermokarst occurrence. We then extrapolated ground-based hotspot flux measurements, observed at the Eastside Pond, to estimate pan-Arctic $CH_4$ fluxes attributable to thermokarst processes. The first approach produced three estimates of daily pan-Arctic Hotspot flux by multiplying ($R_\psi \cdot A_\delta$) by the daily ground-based hotspot mean flux ($F_a$), mean of daily maximum hotspot flux (mean of max flux values from each observation day, $F_b$), and the maximum observed hotspot flux ($F_c$). To convert to annual fluxes, we multiplied the daily fluxes by 200 days $yr^{-1}$ ($t$), to represent the likely annual period of hotspot flux activity.

In our second approach, we estimated a greater $R$ to represent discrete thermokarst features in a more confined area near water bodies ($R_\phi$). Here, $R_\phi$ equaled the integrated $CH_4$ hotspot Poisson rate from terrestrial surfaces within 45 m of open water ($R_\phi = 0.243\%$) from Elder, Thompson, et al. (2020). $R_\phi$ thus represented thermokarst features which were likely to occur within 45 m of water surfaces, a critical distance threshold identified in the 30,000 $km^2$ 2017 AVIRIS-NG AAC (Elder, Thompson, et al., 2020). In this analysis, $R_\phi$ was conservative since it was originally determined with respect to waterbodies in both thermokarst and non-thermokarst areas, where we expect the latter to have fewer hotspots. $R_\phi$ is then multiplied by $A_\beta$, which represented discrete areas of current active/abrupt thaw features (i.e., not inclusive of broader areas where they are likely to occur as in Olefeldt et al. (2016)). Here, $A_\beta$ equaled the area of currently active/abrupt lake thermokarst (78,100 $km^2$, pers. comm. M. Turetsky) plus the area of currently active organic lowland wetland thermokarst (71,700 $km^2$, pers. comm. M. Turetsky) ($A_\beta = 149{,}800$ $km^2$). As in the first approach, the product of $R_\phi \cdot A_\beta$ was then multiplied by $F_a$, $F_b$, $F_c$, and each by $t$ producing three additional estimates of annual pan-Arctic thermokarst hotspot $CH_4$ flux. This calculation and all six flux estimates are summarized in Table 1.

## 3. Results and Discussion

### 3.1. AVIRIS-NG Remote Hotspot Detection

In multiple overflights during July 2018 and 2019, AVIRIS-NG detected persistent $CH_4$ hotspots concentrated on the north eastern margin of the Eastside Pond adjacent to the main body of BTL (Figure 1). While smaller more sporadic hotspots were also detected at other locations around BTL, the area shown in the inset/right panels of Figures 1 and 2 was the only region to consistently show significant $CH_4$ activity (Figure S3 in Supporting Information S1 shows 8 additional AVIRIS-NG images). Specifically, these Eastside Pond hotspots were detected in nine out of 10 surveys flown ≤3,050 m AGL. Above this altitude, hotspots were only observed in two out of seven overflights. This is likely due to dilution of $CH_4$ enhancements over larger image pixels in higher altitude flights. There was no relationship between hotspot detection and sun angle across all flights. Consistent with the findings of Elder, Thompson, et al. (2020), hotspots in general were more concentrated in the nearshore terrestrial environment. The total hotspot area detected by AVIRIS-NG averaged 632 ± 460 $m^2$ within the 50-m-wide littoral + terrestrial perimeter buffer around BTL and the adjacent thermokarst pond, or 0.62 ± 0.45% of the study area (i.e., lake + pond + terrestrial perimeter buffer).

### 3.2. Ground-Based $CH_4$ Observations

Remotely sensed hotspots detected at the Eastside Pond in the morning of 7/6/19 (Figure 1) were confirmed with ground-based enhancement observations approximately 2 hr later on the same day (Figure 2). While most of the ground-based enhancement survey area resembled the area background $CH_4$ concentrations (~1.85 ppm), isolated regions with $CH_4$ concentrations up to 202 ppm were found near to the water's edge (Figure 2). These high concentrations were coincident in space with hotspots that were remotely sensed roughly 2 hr prior (Figures 1 and 2). Plumes of enhanced $CH_4$ (75–100 ppm) were detected several meters inland near the SE portion of the survey, corroborating occasional remote detections 10–20 m from the water's edge. Sporadic ebullition was also visually observed in the water column of the Eastside Pond during periods of the ground-based enhancement survey. It is possible that these emissions from the adjacent water surface (<10 m away) influenced the ground-based enhancement survey, and potentially the remote hotspot detections; however, this effect was not quantified. Ebullition from the adjacent water column has no effect on closed-chamber $CH_4$ flux observations (described in the next section). The peak enhancement of 202 ppm at 0.5 m AGL was applied in the hotspot plume diffusion and advection model to estimate the plume turnover time necessary to produce these conditions at likely hotspot emission rates informed by ground-based flux observations. The results are depicted in Figure S4 in Supporting Information S1, and discussed at the end of this section.

Chamber-based $CH_4$ fluxes within the hotspot region were extreme, but also highly variable, spanning five orders of magnitude ($n = 66$, ranging: 8.5–24,200 mg $CH_4$ $m^{-2}$ $d^{-1}$, Figure 3). These non-ebullitive $CH_4$ hotspot fluxes from the Alaskan Boreal/sub-Arctic are likely some of the highest reported in the scientific literature for northern high latitudes and even rival high diffusive flux observations from tropical wetlands (Nahlik & Mitsch, 2011). The Eastside Pond hotspot overall mean $CH_4$ flux (1,168 mg $CH_4$ $m^{-2}$ $d^{-1}$, $n = 66$), the mean of daily $CH_4$ flux maximum (7,984 mg $CH_4$ $m^{-2}$ $d^{-1}$, $n = 5$), and maximum $CH_4$ flux (24,227 mg $CH_4$ $m^{-2}$ $d^{-1}$, $n = 1$) measured from all 66 observations, represent $F_a$, $F_b$, and $F_c$, respectively in Equation 1 and bracket the likely range of pan-Arctic thermokarst $CH_4$ hotspot fluxes in our pan-Arctic upscaling estimate described below. The median value of observed Eastside Pond hotspot fluxes (218 mg $CH_4$ $m^{-2}$ $d^{-1}$) was excluded in pan-Arctic upscaling since it was unlikely to produce the $CH_4$ enhancements observed at ground level (Figure 2) nor the lower hotspot detection threshold of AVIRIS-NG for this study (≥2,500–3,000 ppm × m $CH_4$) (Equation S3 and Figure S4 in Supporting Information S1). This lower detection threshold is more probable at flux rates comparable or greater than the observed mean of daily maximum fluxes from the Eastside Pond hotspot (~8,000 mg $CH_4$ $m^{-2}$ $d^{-1}$). Despite several extreme flux observations >2,000 mg $CH_4$ $m^{-2}$ $d^{-1}$, Eastside Pond hotspot-region fluxes often resembled high fluxes from other littoral zone locations at BTL (Figure S5 in Supporting Information S1) and the upper range of littoral zone mean fluxes reported in a pan-Arctic synthesis database compiled by Olefeldt et al. (2013) (Figure 3). Despite this variability, a t-test showed that the mean of hotspot fluxes was significantly higher than non-hotspot fluxes at BTL ($p < 0.03$) when aggregating all observations from bare wet shoreline surfaces into the hotspot category (including those observed outside the Eastside Pond hotspot region). Extreme chamber-based fluxes from the Eastside Pond hotspot region extended into at least early winter 2019 and likely beyond, with

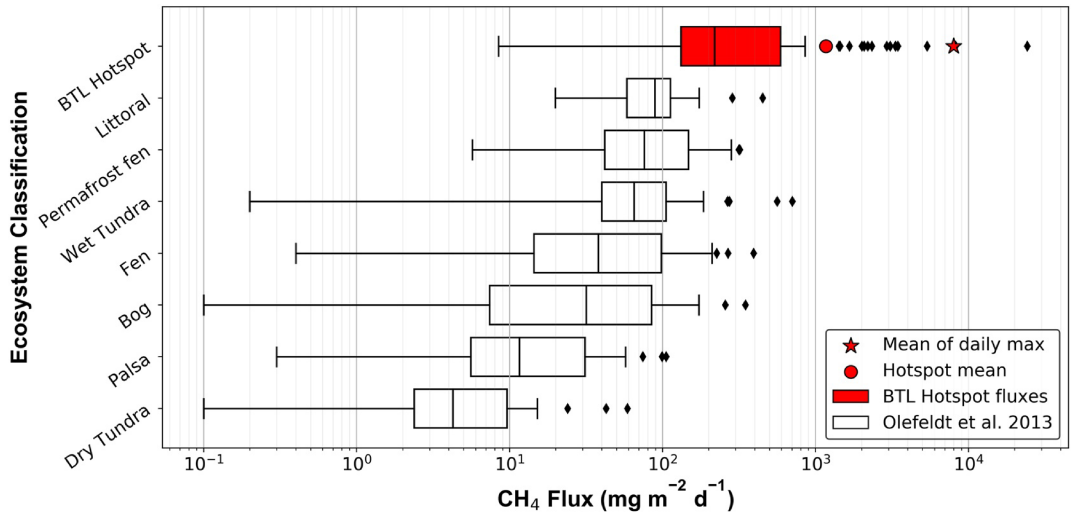


**Figure 3.** Big Trail Lake (BTL) $CH_4$ hotspot fluxes ($n = 66$) compared to distributions of site-level mean fluxes from various ecosystems in a pan-Arctic database. BTL hotspot fluxes were observed from 12 flux monitoring stations located within the remotely observed hotspot on five separate days between 7 July 2019 and 17 September 2019 (see Figure S1 in Supporting Information S1). Database fluxes were taken from Olefeldt et al. (2013).

an observed flux of 1,950 mg $CH_4$ $m^{-2}$ $d^{-1}$ on 14 December 2019, which was greater than the mean of summer measurements (Figure S5 in Supporting Information S1). This prolonged period of activity implicated emission sources from subsurface processes less sensitive to surface freezing or lake-ice formation, perhaps similar to the significant cold season fluxes observed from year-round studies of tundra $CH_4$ fluxes (Zona et al., 2015). This observation informed the 200-day timeframe used for estimating annual hotspot fluxes in our pan-Arctic flux upscaling ($t$ = 200 days $yr^{-1}$, Equation 1).

While AVIRIS-NG's mapping ability enabled precise geolocation (3-m pixels) of the Eastside Pond hotspot in 9 out of 10 lower altitude flights, pinpointing the source of this emission at any given time proved challenging using either our chamber flux monitoring array or ground-based $CH_4$ enhancement survey. Our hotspot flux monitoring array, which was not sampled continuously but sequentially on the day of observations, rarely captured the high spatiotemporal variability of extreme hotspot fluxes within the confined (~3,000 $m^2$) area of the eastern margin of the Eastside Pond. This further emphasizes the importance of high-resolution remote sensing strategies for accurately tracking spatially and temporally sporadic extreme flux events.

Only the highest percentiles of observed hotspot fluxes are likely to result in detection by AVIRIS-NG. This variability presented a challenge for quantifying lower limit of AVIRIS-NG $CH_4$ hotspot detection. To confirm whether the $CH_4$ fluxes from Eastside Pond could generate the 2,500–3,000 ppm × m enhancement needed for confident AVIRIS-NG hotspot detection, we simulated the emissions with a plume diffusion and advection model and a flux of 8,000 mg $CH_4$ $m^{-2}$ $d^{-1}$, roughly equivalent to the mean daily maximum from our in-situ surveys. The model confirmed that this flux rate is detectable with 20–30 min of plume stagnation at the surface (Figure S4 in Supporting Information S1). If we used a flux of 24,000 mg $CH_4$ $m^{-2}$ $d^{-1}$, corresponding to the maximum observed daily flux rate, the 2,500–3,000 ppm × m enhancement threshold accumulated within 3–8 min (Figure S4 in Supporting Information S1). The same plume diffusion and advection model also determined that the maximum observed ground-based enhancement of 202 ppm $CH_4$ (at 0.5 m AGL) would require plume accumulation times of 6 and 2.5 min at the mean of daily maximum and overall maximum observed flux rates, respectively. These results suggest that the flux which produced the hotspot that was detected in the ground-based enhancement survey and in multiple AVIRIS-NG overflights on 7/6/19 was likely closer to 24,000 mg $CH_4$ $m^{-2}$ $d^{-1}$ than to 8,000 mg $CH_4$ $m^{-2}$ $d^{-1}$, and produced a plume that accumulated near the surface for roughly 10 min (Figure S4 in Supporting Information S1). Since this flux magnitude was relatively rare in our ground-based chamber monitoring, we conclude that our monitoring array (collectively covering only ~0.64 $m^2$ with 12 bucket chambers) was likely too sparse to frequently pinpoint the source of hotspot fluxes likely occurring within fractional areas of the 80–150 $m^2$ hotspot plume images produced by AVIRIS-NG. We believe our combined approach of ground-based

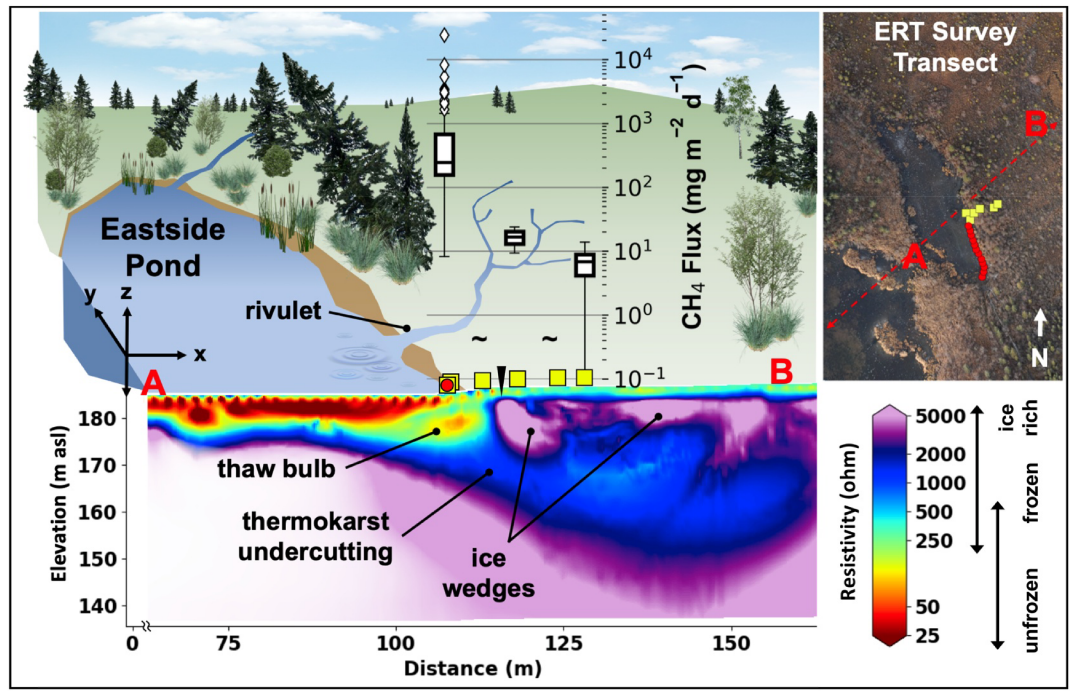


**Figure 4.** Electrical Resistivity Tomography (ERT) cross section identifies a thaw bulb beneath the easternmost shoreline of the Eastside Pond. Subsurface thermokarst features spatially align with extreme $CH_4$ fluxes from the remotely sensed hotspot in the same area (white boxes). The red "A" and "B" correspond to the ERT transect extents in the *x* dimension. A black triangle marks the location of the nuclear magnetic resonance observation. The $CH_4$ flux graph represents data collected between 7 July 2019 and 14 December 2019. Flux data from two long-term monitoring positions (yellow squares) closest to shore were combined with data from the hotspot monitoring positions (red circles) in the first white box of the $CH_4$ boxplot. The "~" symbol represents negligible flux and all symbols are spatially accurate along the *x* dimension.

enhancement mapping, time-series flux monitoring, and plume modeling resulted in the best overall validation of hotspots, however; future studies should consider greater areal coverage for flux monitoring or implementation of drones to more accurately pinpoint $CH_4$ hotspot sources (Oberle et al., 2019).

### 3.3. Geophysical Imaging of Thermokarst Features and $CH_4$ Hotspot Implications

ERT inversion results produced a 2D cross-section through the NE margin of BTL and the Eastside Pond (Figure 4) and four other locations on BTL (Figure S7 in Supporting Information S1). Areas of low resistivity are interpreted as thawed and water-rich sediments, while areas of high resistivity indicate permafrost. Results revealed a prominent low-resistivity thaw bulb directly beneath the NE shoreline of the Eastside Pond to a depth of ~15 m, as well as an intermediate-resistivity undercutting partial thaw feature extending northeastward at depth (Figure 4). The shoreline thaw bulb coincided with the largest observed $CH_4$ fluxes and the remotely sensed hotspots. Fluxes decreased landward, where the ERT results suggested the presence of an intact cap of permafrost between the active layer and the undercutting intermediate-resistivity feature which may contain slightly elevated unfrozen water content. Methane fluxes measured along the separate, permafrost-supported margin on the southern side of BTL, showed a more gradual decline moving away from water (Figure S7 in Supporting Information S1) compared with fluxes measured along the Eastside Pond transect which declined rapidly with distance from shore (Figure 4). For example, fluxes >50 mg $CH_4$ $m^{-2}$ $d^{-1}$ were observed at distances greater than 20 m from the water's edge in the permafrost-supported southern margin of BTL but dropped to undetectable levels within 5 m of the Eastside Pond hotspot shoreline (Figure S7 in Supporting Information S1). In both cases, the magnitude of $CH_4$ flux was correlated with the thickness of thawed sediment identified from the ERT cross-sections. However, the AVIRIS-NG hotspots and extreme chamber fluxes were only observed proximal to the thermokarst features of the Eastside Pond margin where the thawed depth may extend beyond 15 m, which was ~5 m deeper than on BTL's southern margin (Figure 4 and Figure S7 in Supporting Information S1). Although both the Eastside Pond

and southern margin of BTL show relatively deep thaw, more recent thermokarst expansion in the Eastside Pond, compared with the older, stable, permafrost-supported southern margin of BTL, may contribute to this difference given greater availability of more recently thawed permafrost C (Walter Anthony et al., 2018). Differences in thaw age and extent are also supported by the intermediate resistivity values observed in the Eastside Pond talik, indicating partially thawed/frozen sediments, compared with uniformly low resistivity on the southern side of BTL-representative of fully thawed sediments (Figure S7 in Supporting Information S1).

In situ borehole NMR measurements of unfrozen water content with depth just upland of the Eastside Pond lake margin showed approximately 53% volumetric water content (VWC) within the 85 cm active layer (determined with manual frost probe), and residual 1%–9% VWC beneath the active layer to a depth of 2 m (Figure S6 in Supporting Information S1). These data showed there was significant unfrozen pore water in the low-resistivity active layer at this location. The Eastside Pond shoreline thaw bulb at ~15 m depth had low-resistivity values similar to the low-resistivity active layer and likely has comparable unfrozen water content available to support microbial metabolism of permafrost C.

It is likely that the Eastside Pond shoreline talik is contributing to the anomalous $CH_4$ fluxes either by supporting enhanced microbial activity within the saturated and partially thawed shallow sediments, and/or by serving as a pathway connecting water and gases with deeper permafrost C. The latter may represent a preferential flow path for deeper $CH_4$ to reach the atmosphere, similar to hypothesized patterns within lake taliks (Walter et al., 2008), by allowing $CH_4$ to diffuse or advect in thawed channels past the near-surface intact ice wedges and towards the thawed margin at the pond's shoreline. This in effect may concentrate $CH_4$ from a larger subsurface methanogenic volume into a relatively small area of intense, AVIRIS-NG-detectable emissions at the surface. Although we indirectly link potential talik $CH_4$ production and potential deep $CH_4$ channeling via liquid water in the undercutting feature to extreme $CH_4$ flux at the terrestrial surface, collocation of these prominent thermokarst features at the remotely sensed $CH_4$ hotspot support our central hypothesis that these mechanisms promote spatially intensive hotspots of $CH_4$ release to the atmosphere. Ongoing work will utilize isotopic techniques to further investigate the sources of the Eastside Pond $CH_4$ hotspot and explore broader emergent relationships between thermokarst and $CH_4$ hotspots in the domain-wide $CH_4$ hotspot data set.

The localized concentrations of $CH_4$ hotspots in the terrestrial/littoral ecotone we discovered at BTL, and in AVIRIS-NG imagery from across the ABoVE domain, are consistent with the localized concentrations of ebullition hotspots observed within northern lakes (Walter Anthony & Anthony, 2013) and the shallow seas of the Arctic continental shelf (Thornton et al., 2020). In each of these systems, a significant fraction of total $CH_4$ emissions originate from extreme fluxes occurring in disproportionately small areas. Similar to the spatial scarcity of lake ebullition and submerged permafrost $CH_4$ hotspots, terrestrial $CH_4$ hotspots were observed in only ~0.2% of surfaces within 350 m of open water in the total 2017 AVIRIS-NG data set (Elder, Thompson, et al., 2020). While within lake ebullition can be detected visually (bubbling through water, or bubbles incased in winter lake ice), open water surfaces have a SWIR infrared reflectance of <1% which effectively prevented AVIRIS-NG detection of $CH_4$ over these surfaces in our survey, and thus limited AVIRIS-NG's utility for observing within-lake hotspots. Yet, the widespread detection of *invisible* terrestrial hotspot emissions near water in many ABoVE wetland regions is reshaping our understanding of where sites of intense thermokarst-related emissions can occur (Elder, Thompson, et al., 2020). We hypothesize that the same talik-related processes that drive intense, localized $CH_4$ ebullition within the margins of thermokarst water bodies also likely extend into the wet terrestrial nearshore environments, driving more elusive terrestrial hotspot $CH_4$ emissions.

### 3.4. Contextualizing Hotspots Within Total $CH_4$ Emissions at BTL

To contextualize observed $CH_4$ hotspot emissions within total $CH_4$ emissions from the BTL environment, we developed a MESMA-based land surface classification using spectral data for upscaling surface-type-specific fluxes across the study area (Figure 5). This analysis revealed that the hotspots comprised the largest proportion of the BTL study-area diffusive fluxes (39.2%) by a large margin, but accounted for only 0.6% of the BTL study domain (Figure 5). This underscores the disproportionate impact of relatively fine-scale ecological/geomorphological dynamics in site-to-landscape scale $CH_4$ emission upscaling and budgeting. Open water + macrophytes represented the next largest $CH_4$ contribution at roughly 25% of total study area fluxes. Dry grasses + broadleaf surfaces were a small $CH_4$ sink; however, despite comprising 28% of the study area, only offset total study area fluxes by <1%. Since remotely sensed hotspots typically occurred near water, they mostly overlapped with wet

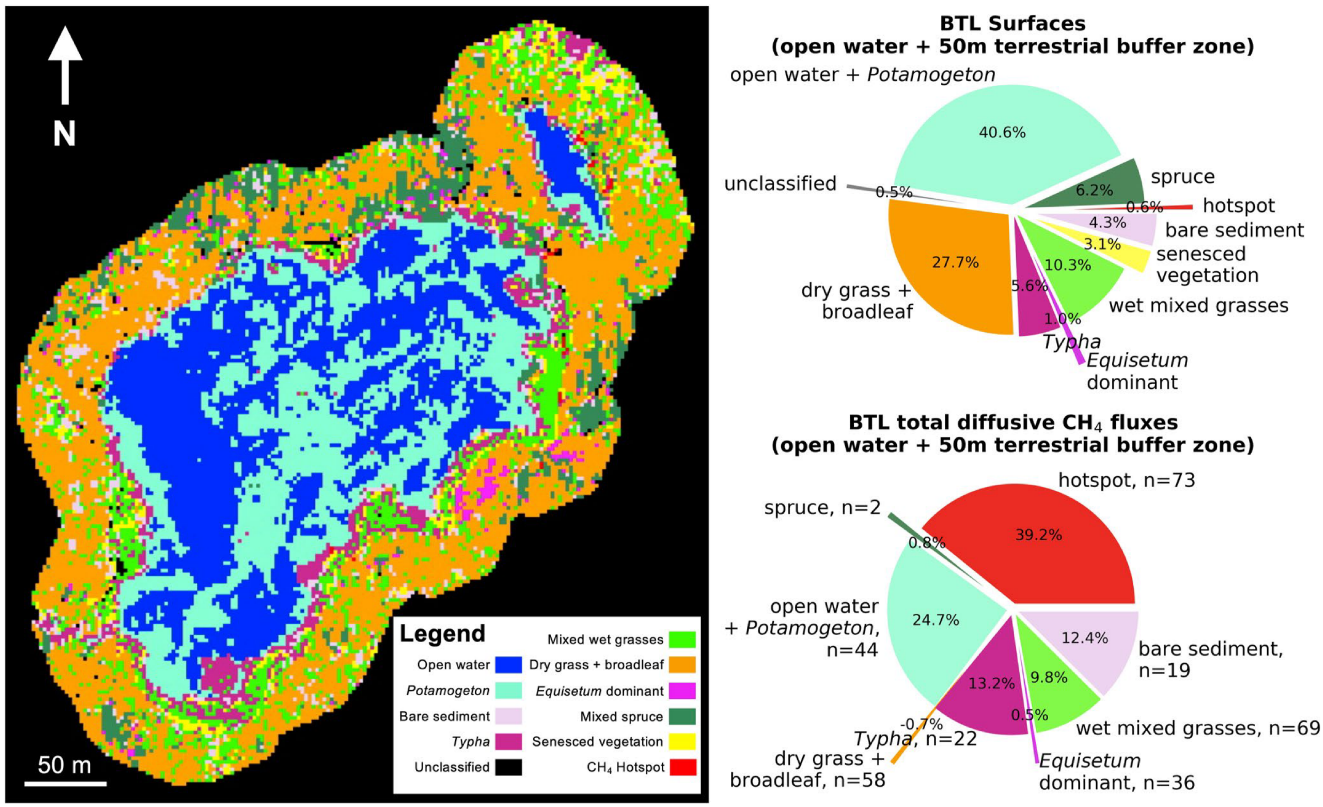


**Figure 5.** Diffusive $CH_4$ flux upscaling at Big Trail Lake using 2018 and 2019 chamber flux measurements and Next Generation Airborne Visible/Infrared Imaging Spectrometer (AVIRIS-NG)-based multiple endmember spectral mixture analysis (MESMA). Ebullition fluxes from the open water and *Potamogeton* areas are high (Walter Anthony et al., 2018), but are not considered in this analysis. The lake map was produced using an AVIRIS-NG reflectance image (2.1 m pixels) and $CH_4$ hotspot detection on 5 July 2019 cropped to the study area. The median of chamber-based $CH_4$ fluxes was determined for each surface type and then multiplied by each surface's area within the map. Hotspots comprised less than 1% of the lake environment, but roughly 40% of the area's total diffusive flux.

bare sediment, *Typha*, and wet mixed grass categories; however, not all of these surfaces were $CH_4$ hotspots at BTL. On rare occasions, hotspots were detected by AVIRIS-NG within the dry grass + broadleaf and spruce surface types. These sporadic hotspots were not targeted for ground validation since they were not spatially consistent in repeated AVIRIS-NG imagery (Figure S3 in Supporting Information S1). It is possible that subsurface talik dynamics near the lake may manifest as sporadic $CH_4$ hotspots on the surface even in areas with less-obvious surficial thermokarst features (i.e., steep slumping shorelines and trees slowly falling into the lake). Enhanced thermokarst, likely caused in part by water flow in multiple rivulets, is the main factor we attribute to the consistent $CH_4$ hotspot behavior at the Eastside Pond.

We estimated total daily diffusive fluxes (including hotspot fluxes) from the 10.2 ha BTL study area (including lake body, Eastside Pond, and 50 m terrestrial buffer zone) to equal 13 kg $CH_4$ $d^{-1}$ during the study period (July 2019). In a separate previously published analysis, BTL open-water ebullition flux was estimated to equal 293 mg $CH_4$ $m^{-2}$ $d^{-1}$ on average (Engram et al., 2020; Walter Anthony et al., 2018). If this ebullition flux is considered in addition total non-ebullitive fluxes estimated here, the total flux (non-ebullition + ebullition) from our study area is roughly doubled to 25 kg $CH_4$ $d^{-1}$. This would also decrease the relative proportion of purely non-ebullitive $CH_4$ flux from Eastside pond hotspots from ~40% to ~20% of total BTL environment emissions, and open water surfaces would overtake hotspots as the greatest contributor to study area $CH_4$ flux (~60% of total)—albeit from an area 40 times larger.

While our MESMA classification only covered BTL and a 50-m terrestrial buffer zone around its perimeter, it demonstrates the value in high-resolution imagery for accurately upscaling $CH_4$ fluxes across heterogeneous environments. Future classifications will exploit full flight line AVIRIS-NG spectral data to produce landscape-scale $CH_4$ flux attribution maps.

To quantify the (dis)proportionality of surface-specific emissions to their representative area at BTL, proportional flux from each individual surface was determined and then divided by its respective proportional coverage (i.e., flux proportion of total/area proportion of total). Table S1 in Supporting Information S1 summarizes the result. Hotspot areas emitted significantly more $CH_4$ per proportional unit area than diffusive fluxes from all other surface types at BTL (i.e., proportional flux >65 times higher than its proportional area at BTL). This supported the hypothesis that large proportions of thermokarst wetland fluxes can originate from disproportionately small areas even at the site scale. The next most disproportionate surfaces were bare wet sediment (2.9 times), then *Typha* (2.4 times). Fluxes from wet mixed grasses were equal in proportion to their area in the study domain (% flux: % area = 1.0), while spruce, *Equisetum* dominant, and dry grass + broadleaf surfaces were underrepresented in $CH_4$ flux per proportional unit area (≤0.5 times). If hotspot fluxes were not considered, flux proportions were 4.7 and 3.8 times greater than the areal proportions for bare sediment and *Typha*, respectively. This implies that if explicit hotspots, like those characterized here, go undetected in a hypothetical emissions survey, but another top-down method of calculating total area flux was used (i.e., eddy covariance), then fluxes from these surfaces could be overestimated by a factor 1.5–2, potentially leading to large discrepancies in further upscaling efforts (Sturtevant & Oechel, 2013).

### 3.5. Upscaling Thermokarst $CH_4$ Hotspot Emissions to the Pan-Arctic

We found that hotspots were up to 2.5 times more likely in wetland and/or lake areas classified as "very high" thermokarst occurrence versus wetland and/or lake areas with low thermokarst occurrence (lower panel of Figure 6). This supports our hypothesis that thermokarst and/or abrupt thaw features promoted the extreme, spatially localized $CH_4$ emissions observed by AVIRIS-NG.

Using our two approaches for estimating pan-Arctic thermokarst $CH_4$ hotspot distribution and flux, we estimate that current thermokarst $CH_4$ hotspot emissions comprise 1.1 Tg $CH_4$ (range: 0.1–5.2 Tg), or roughly 3.6% (0.3%–16.2%), of annual pan-Arctic wetland $CH_4$ emissions (this calculation is summarized in Table 1). This flux originates from a total hotspot area of ~720 $km^2$ or roughly 0.005% of the high latitude permafrost region-a resulting disproportionality ~700 times the proportional flux per proportional area (i.e., % hotspot flux of total: % hotspot area of high latitude permafrost area). This pan-Arctic hotspot flux disproportionality factor (~700) is an order of magnitude greater than the factor of ~65 determined from our MESMA-and flux-chamber-based emissions upscaling of the local BTL environment. This demonstrates that thermokarst $CH_4$ emission hotspots act as islands of exponentially disproportionate $CH_4$ emissions on spatial scales extending beyond lake and proximal wetland environments.

### 3.6. Caveats to Upscaling Pan-Arctic Hotspot Fluxes

Detectability of $CH_4$ hotspot fluxes by AVIRIS-NG is primarily a function of flux magnitude and wind speed (or plume stagnation), where higher wind speeds diminish $CH_4$ enhancement and detectability. Alternatively, lower fluxes may be detectable where surface roughness, caused by standing vegetation or microtopography (common in the permafrost domain), result in near-surface air stagnation and $CH_4$ accumulation over longer periods. Despite the high spatiotemporal variability of these factors across the high northern latitudes, our diffusion and advection plume model (Figure S4 in Supporting Information S1) showed that the flux rates observed from the Eastside Pond margin (5,000–24,000 mg $CH_4$ $m^{-2}$ $d^{-1}$) and plausible plume turnover (stagnation) times of 5–20 min lead to hotspots that could be detected by AVIRIS-NG. These conditions are consistent with the very low wind conditions common at BTL during the clear-sky summer days when AVIRIS-NG typically acquired imagery. These low-wind conditions, which were confirmed by wind observations at the eddy covariance tower on BTL (commonly <1.5 m/s during overflights), are characteristic of potential "clear sky bias" weather conditions which apply to all AVIRIS-NG scenes. This bias could increase the sensitivity of AVIRIS-NG to lower flux rates if low windspeed and greater air stagnation, particularly in sheltered environments, allowed enhancements to accumulate to higher concentrations at ground level. As a result, upscaled pan-Arctic thermokarst fluxes based on our BTL observations, may be overestimated. However, this effect is likely more than counterbalanced by two other aspects of the survey which render our pan-Arctic emission estimate more conservative. First, the Eastside Pond hotspot was only detected in 30% of higher-altitude AVIRIS-NG flights (>3,050 m AGL), which is more representative of the ~5,000 m AGL altitude in the broader ABoVE surveys. Thus, hotspots with the flux magnitude similar to that of the Eastside Pond hotspot were more often undetected in the broader survey. This would

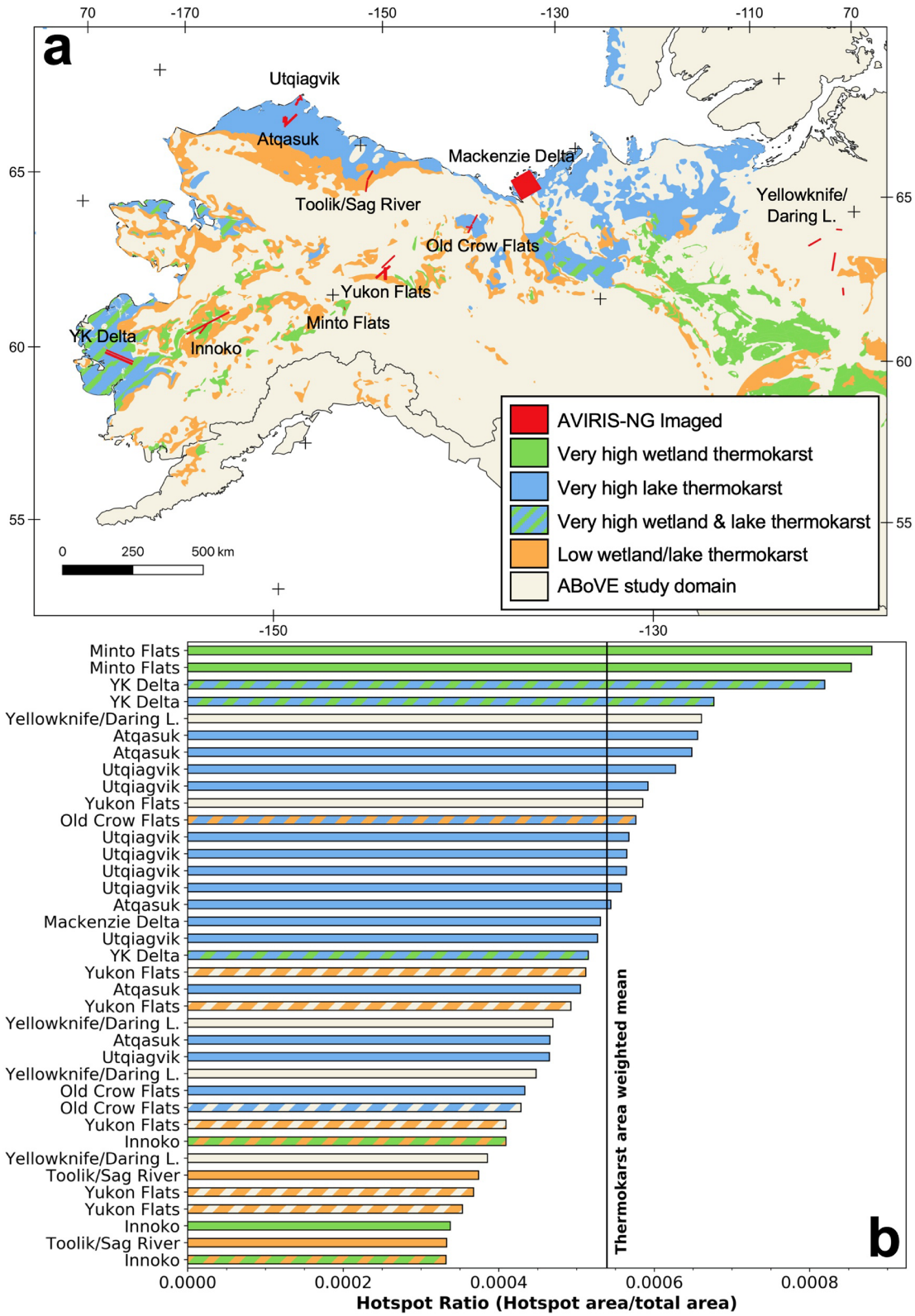


**Figure 6.** Hotspot ratios by region. (a) Subset of 64 Next Generation Airborne Visible/Infrared Imaging Spectrometer (AVIRIS-NG) flight lines from 2017 to 2019 mapped in relation to either "very high," intermediate, or "low" thermokarst characteristics classified by Olefeldt et al. (2016). (b) AVIRIS-NG-based $CH_4$ hotspot occurrence ratio (used to calculate $R_\psi$ in Equation 1) ranked for each flight line (Mackenzie Delta mosaic plotted as a single bar). Bars are color-coded based on map legend.

effectively reduce the total number of detected hotspots and reduce our pan-Arctic hotspot emissions estimate. Second, AVIRIS-NG is not sensitive to $CH_4$ enhancements over water surfaces due to their low reflectivity in the SWIR infrared wavelengths used for the $CH_4$ retrieval. Thus, AVIRIS-NG does not capture complete thermokarst flux variability in space, time, and magnitude, especially in regions with one-off or infrequent overflights. This would further reduce the frequency of hotspots in our survey and our upscaled hotspot emissions estimate.

Since ebullition was frequently observed in the water <10m (and upwind) from the AVIRIS-NG detected hotspots at the Eastside Pond, it is possible that these water-borne emissions occasionally combined with detectable fluxes observed from the adjacent SWIR-reflective land surface and/or nearby plant-mediated fluxes to promote local $CH_4$ enhancements to the lower AVIRIS-NG detection limit. If this effect is widespread in the ABoVE AVIRIS-NG surveys, it means our surveys remain sensitive to regions where ebullition is strong enough and close enough to land (typical of lake thermokarst margins) to be detected. This would also likely lead to an underestimation of the spatial extent and flux rates necessary to render such an enhancement. This effect, combined with the inability to observe lower-level water fluxes with plumes that do not extend over land, or higher fluxes further from the SWIR-reflective surfaces of land, further supports the conservatism of our pan-Arctic upscaling.

We did not quantify these effects, but we believe this variability is captured in our estimated range of annual $CH_4$ flux from thermokarst features (0.1–5.2 Tg $CH_4$ $yr^{-1}$). Despite this wide range, our two independent approaches overlap between 0.3 and 1.8 Tg $CH_4$ $yr^{-1}$ (median across all estimates = 1.1 Tg $CH_4$ $yr^{-1}$, Table 1). Although this estimate carries relatively large uncertainty, it is conservative and it exploits our novel $CH_4$ hotspot survey, which spans spatial scales from 25 $m^2$ to 70,000 $km^2$, and represents a unique observation-based apportionment of $CH_4$ fluxes to complex and climate-sensitive thermokarst processes. This estimate could serve both as an important baseline for monitoring future $CH_4$ emissions from accelerating permafrost thaw, and a tool to potentially allocate thermokarst emissions in top-down and bottom-up emission accounting and projections.

Aside from ground-based determination of flux magnitudes required to produce an AVIRIS-NG $CH_4$ hotspot, our approaches to upscaling $CH_4$ fluxes to pan-Arctic thermokarst processes leveraged the ability of AVIRIS-NG to determine hotspot areal coverage relative to total imaged area (hotspot occurrence ratio) at very high spatial resolution (25 $m^2$ pixels) over more than nine orders of magnitude of surveyed area (nearly 100,000 $km^2$ imaged through 2019). Despite this unprecedented sampling across spatial scales, direct determination of total pan-Arctic hotspot area was not possible. Thus, our approaches rely on two key assumptions. First, all hotspot areas, despite quantitative AVIRIS-NG $CH_4$ enhancement variability, were assigned the same flux value in each respective upscaling approach. This equates to the assumption that the flux values observed at the Eastside Pond are representative of hotspot fluxes across the Arctic. Second, we assume that thermokarst processes like those observed at BTL produce all hotspot emissions within the upscaling regions defined by our two approaches. A formal quantitative analysis of the uncertainty brought by these assumptions is beyond the scope of this study. However, we posit that the likely range of pan-Arctic thermokarst $CH_4$ hotspot emissions is bracketed by our multiple independent upscaling approaches.

Our two approaches differ in the way that they estimate the total area of Arctic thermokarst features. The first approach, estimates the fraction of thermokarst within the entire mapped area of very high wetland and/or thermokarst occurrence determined by Olefeldt et al. (2016), while the second method directly estimates discrete areas of thermokarst features (M. Turetsky, pers. comm.). The first approach likely overestimates the area corresponding to thermokarst-driven hotspots; however, we expect this overestimation to be counterbalanced by the likelihood that the second approach underestimates hotspot occurrence-since the hotspot occurrence ratio we applied was determined in large part from areas without thermokarst features. For example, hotspots in the BTL study area (representing a young/active thermokarst environment) occurred in 0.62 ± 0.45% of the study area, while the hotspot fractional area used for discrete pan-Arctic thermokarst features was almost three times less (0.243%, Table 1). Nevertheless, we believe that the median pan-Arctic flux estimate of 1.1 Tg $CH_4$ $yr^{-1}$ from all of our upscaling approaches is conservative since it falls in the range where our estimates overlap.

It is likely that the mechanisms that regulate episodic ebullition events within the water columns of lakes also exist in the adjacent nearshore terrestrial environment. However, a key difference is that these pulse-like emissions in the saturated, but not inundated, near-shore environment likely more closely resemble periodically high rates of diffusion instead of the abrupt emissions characteristic of ebullition events in water. While the temporal variability of these pulse-like diffusive fluxes was not well constrained in our study, this mechanism may explain

why extreme fluxes detectable by AVIRIS-NG were only occasionally observed in our chamber-based flux monitoring at the Eastside Pond. As discussed in Windsor et al. (1992), it is possible that episodic ebullition-like releases of $CH_4$, originating from deeper, saturated sediments, are transformed by the overlying soil/sediment matrix along waterbody margins into more diffuse emission modes. Indeed, our observed extreme diffusion rates (mean: 1,110 mg $CH_4$ $m^{-2}$ $d^{-1}$, $n = 65$) closely resemble high ebullition-flux rates previously observed from young/active Yedoma thermokarst lakes in Siberia and Alaska (Sepulveda-Jauregui et al., 2015; Walter Anthony et al., 2010, 2016). Although rapid (i.e., order of seconds to tens of seconds), non-linear concentration increases were occasionally observed within the hotspot monitoring chambers, these measurements were discarded due to the potential that even small chamber agitations during measurement could trigger artificial emission events in the sensitive sediments. Considering this, our measurements of extreme hotspot flux rates only represent linear diffusion rates which occur for a minimum of 45 s, and thus could underestimate total hotspot flux if more rapid ebullition-like events also occur in the terrestrial sediments of the nearshore environment. This uncertainty is likely captured in the range of pan-Arctic emissions estimates derived from our comprehensive spatial sampling via AVIRIS-NG and our thermokarst upscaling approaches. However, in the context of our MESMA-based upscaling of surface-specific fluxes at BTL (Figure 5), ebullition was not considered, meaning a significant fraction of $CH_4$ flux (specifically via ebullition from open water at BTL) was not included in the BTL study area proportional flux analysis (Table S1 in Supporting Information S1).

### 3.7. Origins of $CH_4$ Hotspots

On the surface above the Eastside Pond talik, several small rivulet streams each created 1–2 m deep depressions, elongated 3–6 m to the east and perpendicular to the main axis of the Eastside pond. The rivulets with more consistent water flow appeared to spatially correlate with high fluxes, detected hotspots, and ERT-observed subsurface thermokarst features. These depressions may reflect voids that were previously occupied by massive ice wedges, like those observed subsurface and to the east of the Eastside Pond in the ERT cross-section (Figure 4). The degradation of ice wedges likely accelerates thermokarst at the Eastside Pond and promotes enhanced mineralization of permafrost C to $CH_4$ in the subsurface. Furthermore, the surface depressions are somewhat sheltered from ventilation, creating ideal conditions for air stagnation and $CH_4$ accumulation near the surface. Hydrophytic vegetation, while not unique to the Eastside Pond, is abundant on its margins and may combine with supplemental permafrost-C-sourced $CH_4$ to elevate emissions through vascular plant tissues (Andresen et al., 2017; Ström et al., 2003), though this effect was not directly quantified.

Further characterization of the origins of remotely detected $CH_4$ hotspots would greatly benefit from isotopic analysis ($\Delta^{14}C$, $\delta^{13}C$, $\delta D$, clumped isotopes) of the emitted gas. Such analysis would improve apportionment of hotspot fluxes potentially originating both ancient permafrost C or from sub-permafrost, geologic C sources (Douglas et al., 2020; Walter Anthony et al., 2012), which are known to exist in portions of the broader ABoVE domain. However, given the 2 million $CH_4$ hotspots detected by AVIRIS-NG across the surveyed area of the ABoVE domain (Elder, Thompson, et al., 2020), ecologic C (permafrost C and/or actively cycling surface C) likely dominate hotspot emission sources. Future ground-based investigations of AVIRIS-NG-detected hotspots would also benefit from subsurface dissolved gas observations and diffusive modeling. These observations could further elucidate the methanogenic horizons most responsible for anomalous $CH_4$ emission at the surface (Wickland et al., 2006). As such, the AVIRIS-NG $CH_4$ survey is a valuable tool to guide more intensive ground-based investigations toward sites of extraordinary $CH_4$ emissions.

### 3.8. Regional $CH_4$ Hotspot Patterns

While it is difficult to determine whether thermokarst features like those at BTL are the predominant driver of $CH_4$ hotspot occurrence in the broader AVIRIS-NG survey, we suspect this to be the case given the increased likelihood of hotspot occurrence in very high versus low thermokarst environments (Figure 6). Our observations of high $CH_4$ hotspot activity, particularly in the Yukon-Kuskokwim Delta and Alaskan North Slope (Figure 6), correspond to elevated $CH_4$ emissions in the same regions as determined from inverse modeling of airborne concentration data (S. M. Miller et al., 2016). This suggests that $CH_4$ hotspots may be the dominant mode of $CH_4$ emission in regions that are conducive to thermokarst. While outside the scope of this study, future work will focus on more quantitative comparisons between AVIRIS-NG hotspot patterns and other complementary airborne

(Kohnert et al., 2018; Miller et al., 2016; Sweeney et al., 2020) and spaceborne $CH_4$ remote sensing observations (Engram et al., 2020).

The Innoko wetlands proved an exception to the patterns shown in Figure 6. Reasons for the low hotspot occurrence in the Innoko wetlands are unexplained, especially since high fluxes are expected from this peaty-silty lowland region riddled with collapse-scar bogs and fens (Torre Jorgenson et al., 2013). The observation could relate to lower densities of AVIRIS-NG-detectable extreme emission sites within networks of older (>200 years) collapse bogs which are known to have lower $CH_4$ emissions in the region (Johnston et al., 2014). Innoko $CH_4$ hotspot activity was also potentially suppressed by local environmental/meteorological conditions on the day of observation.

### 3.9. Implications for Current and Future Pan-Arctic $CH_4$ Emissions

While our best estimate of $CH_4$ flux from pan-Arctic thermokarst is only around 4% (1.1 Tg $CH_4$ $yr^{-1}$) of total estimated pan-Arctic wetland emissions (32 Tg $CH_4$ $yr^{-1}$, sans lake emissions (Peltola et al., 2019)), it may represent a previously unaccounted source within pan-Arctic emission budgeting. Given the high uncertainty range of our estimate (range 0.1–5.2 Tg $CH_4$ $yr^{-1}$), thermokarst may be responsible for substantially more than (or less than) 1.1 Tg $CH_4$ emissions annually.

We believe that the hotspot emissions represented here, and particularly their widespread occurrence, have until now gone mostly unobserved and undescribed. Without the ability to observe extreme *terrestrial* flux events at high spatial resolution and broad coverage, and with limited datasets of high-spatial-resolution $CH_4$ flux observations (i.e., spatially confined chamber fluxes) from thermokarst environments, such events likely went undetected prior to the AVIRIS-NG survey. However, it is also safe to assume that not all thermokarst environments are capable of emitting $CH_4$ at high enough rates to meet the AVIRIS-NG hotspot threshold definition (likely 5–15 g $CH_4$ $m^{-2}$ $d^{-1}$ given plausible plume turnover times). If hotspots, like those characterized here, were undetected and unaccounted in previous research, our estimate would, in effect, increase bottom-up flux estimates and widen their discrepancy with top-down emission accounting. For example, Walter Anthony et al. (2016) estimates emissions of 2.2–6.7 Tg $CH_4$ $yr^{-1}$ from thermokarst lake margin expansion during the last 60 years. However, this estimate does not include hotspot fluxes from the nearshore terrestrial environment, a buffer zone extending from the water's edge where Elder, Thompson, et al. (2020) showed that hotspots are most likely to occur within 45 m of the shoreline. Our results suggest that the 2.2–6.7 Tg $CH_4$ $yr^{-1}$ estimate from lake thermokarst expansion zones could be underestimated by 25%–50% since nearshore terrestrial hotspots were not considered.

Bottom-up accounting typically estimates double the pan-Arctic emissions of top-down methods (59.7 (36.9–89.4) versus 23 ± 5 Tg $CH_4$ $yr^{-1}$, respectively, including lake flux (Thornton et al., 2016)). Given the high uncertainty in both accounting approaches, it is plausible that terrestrial thermokarst $CH_4$ hotspots account for a "newly known" emission mode of around 1.1 (0.1–5.2) Tg $CH_4$ $yr^{-1}$ in the pan-Arctic budget- and would imply a mis-apportionment of $CH_4$ fluxes within bottom-up budgeting efforts. It is likely that many bottom-up emission estimates do not accurately account for the areal disproportionality of $CH_4$ hotspot fluxes within emitting surfaces and over-allocate elevated flux rates during upscaling to areas that actually emit much less $CH_4$. This leads to an overestimation of the contributing area to total study domain emissions, which is consistent with the propensity of bottom-up emissions accounting to overshoot top-down constraints (Thornton et al., 2016). A solution to the problem of over-allocating emissions to surfaces without accounting for the finer-scale spatial heterogeneity brought by hotspot behavior will require complementary high-resolution observations and land surface modeling over large scales. This concept was demonstrated when a up to a 60% reduction in total $CH_4$ fluxes was observed when land surface model resolution was increased to finer spatial scales (Treat et al., 2018). In another example, regional lake $CH_4$ emissions, based on high-resolution satellite remote sensing analyses, were lower compared to previous estimates based on upscaling from individual lakes (Engram et al., 2020). The high-spatial resolution $CH_4$ hotspot mapping ability of AVIRIS-NG has the potential to improve $CH_4$ upscaling efforts by explicitly defining the areal extent of high emission sites.

Although the hotspots described in this work may be a newly known $CH_4$ source to the atmosphere, at the current state of our collective understanding, it appears impossible to determine whether this source is truly new with respect to the Arctic's response to recent warming. Despite this incomplete understanding, our estimate serves as

an important starting point to motivate further investigation into thermokarst $CH_4$ emissions across the warming pan-Arctic region.

If thermokarst $CH_4$ hotspot emissions are sourced primarily from ancient permafrost C reservoirs, they likely also represent a new source to actively cycling C at the surface and an enhancement to the positive C-climate feedback to further atmospheric warming. While this effect remains difficult to quantify, recent model estimates suggest that thousands of Tg of $CH_4$ could be released from abruptly thawing permafrost under RCP 8.5 warming scenarios by the end of the century (Turetsky et al., 2020). The resulting increase in net radiative forcing by year 2300 (0.15 W $m^{-2}$) would represent roughly 1/3 of all $CH_4$-driven radiative forcing since 1750 (0.48 ± 0.05 W $m^{-2}$) (Myhre et al., 2013). Even on shorter time horizons and regardless of the emission source, increases in intense $CH_4$ hotspot emissions from thawing permafrost like those described here are likely to further offset the long-term cooling effect of $CO_2$ uptake by these ecosystems. This would further increase their hypothesized net positive warming effect though year 2100 (Helbig et al., 2017). These potential impacts emphasize the importance of improving monitoring capabilities for detecting and attributing permafrost C losses, especially as $CH_4$.

## 4. Conclusions

We combined airborne and ground-based observations to quantify thermokarst $CH_4$ emissions on scales bridging chamber flux observations (<1 $m^2$), plot-level monitoring (10–1,000 of $m^2$), and thermokarst lake ecosystem flux budgeting (1–5 ha). Leveraging regional $CH_4$ hotpot statistics from our 70,000 $km^2$ (7 Mha) AVIRIS-NG survey across Alaska and northwestern Canada, we extrapolated our results to the terrestrial pan-Arctic (18 $Mkm^2$).

Repeat AVIRIS-NG airborne measurements were used to detect a persistent, previously undiscovered $CH_4$ hotspot along the shore of the Eastside Pond, an arm of Big Trail Lake, an intensively studied thermokarst lake in Interior Alaska (Figure 1). Flux chamber measurements validated the remote hotspot detection, yielding a mean daily flux of 1,170 mg $CH_4$ $m^{-2}$ $d^{-1}$, with daily maxima extending up to an extreme value of 24,200 mg $CH_4$ $m^{-2}$ $d^{-1}$ (Figures 2 and 3, Table 1). Ground-based geophysical surveys of the BTL and Eastside Pond environment confirmed the presence of actively thawing permafrost collocated at the $CH_4$ hotspot (Figure 4). We performed an image classification of the BTL study area using AVIRIS-NG imagery, and used the resulting map to apportion multiyear chamber-based $CH_4$ fluxes to the nine unique surface types observed in the lake and nearshore environment (Figure 5). This analysis contextualized hotspot fluxes within the broader lake environment, where we found that they comprised 40% of the study area diffusive $CH_4$ emissions despite arising from less than 1% of the total study area.

An analysis of 64 AVIRIS-NG flight lines acquired during the AAC in 2017, 2018, and 2019 (C. E. Miller et al., 2019; Elder, Thompson, et al., 2020) revealed greater hotspot occurrence in regions exhibiting very high wetland and/or lake thermokarst occurrence (Figure 6). These hotspots all corresponded to $CH_4$ signals as large or larger than those observed from the Big Trail Lake hotspot. The relative fractions of $CH_4$ hotspot area in the lower panel of Figure 6 support our hypothesis that thermokarst processes promote extreme $CH_4$ emissions from disproportionately small areas in the Arctic permafrost landscape. To estimate $CH_4$ hotspot emissions from thermokarst regions across the pan-Arctic, we combined three flux rates observed from the Eastside Pond thermokarst hotspot with domain-wide hotspot occurrence statistics derived from the 70,000 $km^2$ AVIRIS-NG survey. We conservatively estimate that thermokarst hotspots emit roughly 1.1 Tg $CH_4$ $yr^{-1}$ or roughly 4% of the current pan-Arctic wetland budget based on two independent estimation approaches.

This investigation highlights the unique insights made possible from the nine orders of magnitude in spatial scales sampled by the AVIRIS-NG airborne $CH_4$ hotspot imagery. Individual pixels (typically 25 $m^2$ or $2.5 \times 10^{-5}$ $km^2$) resolve fine-scale geomorphological drivers while composite maps (1,000–10,000 $km^2$) enable the evaluation of climatic-scale influence on $CH_4$ emissions. The opportunity to simultaneously analyze hotspot patterns and statistics across site, landscape, and regional spatial scales enables us to characterize emergent properties and verify upscaling assumptions directly with observational data. One can also derive land surface classifications as well as vegetation traits and taxonomy from the same AVIRIS-NG pixels used to retrieve the $CH_4$ hotspots, resulting in exact collocation of these properties for correlation studies of unprecedented detail. Continued observations and incorporation of complementary methods (i.e., airborne eddy covariance) are needed to reduce uncertainties in pan-Arctic hotspot emission estimates. Yet, our initial analyses build confidence that these types of multi-scale studies will help us overcome the scaling challenges that have long hindered accurate estimates of the Arctic

$CH_4$ budget (McGuire et al., 2012, 2018). We continue to explore all dimensions of the AVIRIS-NG $CH_4$ hotspot data set and anticipate more discoveries as we investigate biotic (i.e., vegetation, microbial, beaver activity, etc.) and abiotic (i.e., fire, hydrology, surficial geology, geomorphology, etc.) responses to thawing permafrost in a warming world.

## Conflict of Interest

The authors declare no conflicts of interest relevant to this study.

## Data Availability Statement

AVIRIS-NG level 1 and level 2 radiance data are available via the Oak Ridge National Laboratory Distributed Active Archive Center (ORNL DAAC) at Miller et al. (2019). In situ 2019 $CH_4$ flux data is published at ORNL DAAC (Elder et al., 2021).

**Acknowledgments**
The authors would like to thank Michael Eastwood (JPL), John Chapman (JPL), Mark Helmlinger (JPL), and the rest of the AVIRIS-NG technical support and flight crew for spectroscopic data acquisition from the air and the ground. The authors thank the Alaska Satellite Facility (University of Alaska Fairbanks) for expedient AVIRIS-NG data transfer to servers at JPL, which enabled overnight detection of $CH_4$ hotspots at BTL. The authors acknowledge our ABoVE collaborators, David Butman (University of Washington), Mark Dornblaser (USGS), Kim Wickland (USGS), Rob Striegl (USGS), Catherine Kuhn (University of Washington), and Merritt Turetsky (University of Colorado) for their valuable feedback regarding several aspects of this work. The authors also thank Sarah Sackett and Dan Hodgkinson for logistical assistance through the ABoVE Fairbanks office. NASA funding was provided to PI C. E. Miller from the Terrestrial Ecology Program via ABoVE and C. D. Elder via USRA and the NASA Postdoctoral Program. USGS funding was provided by the USGS Land Change Science and Biological Sequestration Programs.  The research was carried out at the Jet Propulsion Laboratory, California Institute of Technology, under a contract with the National Aeronautics and Space Administration.

## References

Andresen, C. G., Lara, M. J., Tweedie, C. E., & Lougheed, V. L. (2017). Rising plant-mediated methane emissions from arctic wetlands. *Global Change Biology*, *23*(3), 1128–1139. https://doi.org/10.1111/gcb.13469

Bloom, A. A., Bowman, K. W., Lee, M., Turner, A. J., Schroeder, R., Worden, J. R., et al. (2017). A global wetland methane emissions and uncertainty dataset for atmospheric chemical transport models (WetCHARTs version 1.0). *Geoscientific Model Development*, *10*(6), 2141–2156. https://doi.org/10.5194/gmd-10-2141-2017

Briggs, M. A., Campbell, S., Nolan, J., Walvoord, M. A., Ntarlagiannis, D., Day-Lewis, F. D., & Lane, J. W. (2017). Surface geophysical methods for characterising frozen ground in transitional permafrost landscapes. *Permafrost and Periglacial Processes*, *28*(1), 52–65. https://doi.org/10.1002/ppp.1893

Cooper, M. D. A., Estop-Aragonés, C., Fisher, J. P., Thierry, A., Garnett, M. H., Charman, D. J., et al. (2017). Limited contribution of permafrost carbon to methane release from thawing peatlands. *Nature Climate Change*, *7*(7), 507–511. https://doi.org/10.1038/nclimate3328

Cusworth, D. H., Duren, R. M., Thorpe, A. K., Tseng, E., Thompson, D. R., Guha, A., et al. (2020). Using remote sensing to detect, validate, and quantify methane emissions from California solid waste operations. *Environmental Research Letters*, *15*(5). https://doi.org/10.1088/1748-9326/ab7b99

Dean, J. F., Meisel, O. H., Martyn Rosco, M., Marchesini, L. B., Garnett, M. H., Lenderink, H., et al. (2020). East Siberian Arctic inland waters emit mostly contemporary carbon. *Nature Communications*, *11*(1), 1–10. https://doi.org/10.1038/s41467-020-15511-6

Douglas, P. M. J., Gonzalez Moguel, R., Walter Anthony, K. M., Wik, M., Crill, P. M., Dawson, K. S., et al. (2020). Clumped isotopes link older carbon substrates with slower rates of methanogenesis in Northern Lakes. *Geophysical Research Letters*, *47*(6), 1–10. https://doi.org/10.1029/2019GL086756

Duren, R. M., Thorpe, A. K., Foster, K. T., Rafiq, T., Hopkins, F. M., Yadav, V., et al. (2019). California's methane super-emitters. *Nature*, *575*(7781), 180–184. https://doi.org/10.1038/s41586-019-1720-3

Elder, C., Hasson, N., Hanke, P., Wright, S., Anthony, K. W., & Miller, C. E. (2021). Methane fluxes from shorelines and differing surfaces, big Trail Lake, Alaska, 2019. ORNL DAAC. https://doi.org/10.3334/ORNLDAAC/1870

Elder, C. D., Hanke, P. J., Walter Anthony, K. M., Thompson, D. R., Thorpe, A. K. & Miller, C. E. (2020). ABoVE: Methane flux across two thermokarst lake ecosystems, interior Alaska, 2018. https://doi.org/10.3334/ORNLDAAC/1778

Elder, C. D., Thompson, D. R., Thorpe, A. K., Hanke, P., Walter Anthony, K. M., & Miller, C. E. (2020). Airborne mapping reveals emergent power law of arctic methane emissions. *Geophysical Research Letters*, *47*(3). https://doi.org/10.1029/2019GL085707

Elder, C. D., Xu, X., Walker, J., Schnell, J. L., Hinkel, K. M., Townsend-Small, A., et al. (2018). Greenhouse gas emissions from diverse Arctic Alaskan lakes are dominated by young carbon. *Nature Climate Change*, *8*(2), 166–177. https://doi.org/10.1038/s41558-017-0066-9

Engram, M., Walter Anthony, K. M., Sachs, T., Kohnert, K., Serafimovich, A., Grosse, G., & Meyer, F. J. (2020). Remote sensing northern lake methane ebullition. *Nature Climate Change*, *10*(6), 511–517. https://doi.org/10.1038/s41558-020-0762-8

Farquharson, L. M., Romanovsky, V. E., Cable, W. L., Walker, D. A., Kokelj, S. V., & Nicolsky, D. (2019). Climate change drives widespread and rapid thermokarst development in very cold permafrost in the Canadian High Arctic. *Geophysical Research Letters*, *46*(12), 6681–6689. https://doi.org/10.1029/2019GL082187

Frankenberg, C., Thorpe, A. K., Thompson, D. R., Hulley, G., Kort, E. A., Vance, N., et al. (2016). Airborne methane remote measurements reveal heavy-tail flux distribution in Four Corners region. *Proceedings of the National Academy of Sciences*, *113*(35), 201605617. https://doi.org/10.1073/pnas.1605617113

Helbig, M., Chasmer, L. E., Kljun, N. C., Quinton, W. L., Treat, C. C., & Sonnentag, O. (2017). The positive net radiative greenhouse gas forcing of increasing methane emissions from a thawing boreal forest-wetland landscape. *Global Change Biology*, *23*(6), 2413–2427. https://doi.org/10.1111/gcb.13520

James, S. R., Minsley, B. J., Pastick, N. J., & Sullivan, T. D. (2020). Alaska permafrost characterization: Geophysical and related field data collected from 2019–2020: U.S. Geological Survey. https://doi.org/10.5066/P9I6VUQV

Johnston, C. E., Ewing, S. A., Harden, J. W., Varner, R. K., Wickland, K. P., Koch, J. C., et al. (2014). Effect of permafrost thaw on $CO_2$ and $CH_4$ exchange in a western Alaska peatland chronosequence. *Environmental Research Letters*, *9*(10), 109601. https://doi.org/10.1088/1748-9326/9/10/109601

Kohnert, K., Juhls, B., Muster, S., Antonova, S., Serafimovich, A., Metzger, S., et al. (2018). Toward understanding the contribution of waterbodies to the methane emissions of a permafrost landscape on a regional scale – A case study from the Mackenzie Delta, Canada. *Global Change Biology*, 1–14. https://doi.org/10.1111/gcb.14289

Lewkowicz, A. G., Etzelmüller, B., & Smith, S. L. (2016). Characteristics of discontinuous permafrost based on ground temperature measurements and electrical resistivity tomography, Southern Yukon, Canada. *Permafrost and Periglacial Processes*, *22*(4), 320–342. https://doi.org/10.1002/ppp.703

Lewkowicz, A. G., & Way, R. G. (2019). Extremes of summer climate trigger thousands of thermokarst landslides in a High Arctic environment. *Nature Communications*, *10*(1), 1–11. https://doi.org/10.1038/s41467-019-09314-7

McGuire, A. D., Christensen, T. R., Hayes, D., Heroult, A., Euskirchen, E., Kimball, J. S., et al. (2012). An assessment of the carbon balance of Arctic tundra: Comparisons among observations, process models, and atmospheric inversions. *Biogeosciences*, *9*(8), 3185–3204. https://doi.org/10.5194/bg-9-3185-2012

McGuire, A. D., Lawrence, D. M., Koven, C., Clein, J. S., Burke, E., Chen, G., et al. (2018). Dependence of the evolution of carbon dynamics in the northern permafrost region on the trajectory of climate change. *Proceedings of the National Academy of Sciences of the United States of America*, *115*(15), 3882–3887. https://doi.org/10.1073/pnas.1719903115

Miller, C. E., Green, R. O., Thompson, A. K., Thorpe, M., Eastwood, I. B., Mccubbin, W., et al. (2019). ABoVE: Hyperspectral imagery from AVIRIS-NG, Alaskan and Canadian Arctic, 2017–2019. ORNL DAAC. https://doi.org/10.3334/ORNLDAAC/1569

Miller, C. E., Griffith, P. C., Goetz, S. J., Hoy, E. E., Pinto, N., McCubbin, I. B., et al. (2019). An overview of ABoVE airborne campaign data acquisitions and science opportunities. *Environmental Research Letters*, *14*, 080201. https://doi.org/10.1088/1748-9326/ab0d44

Miller, S. M., Miller, C. E., Commane, R., Chang, R. Y. W., Dinardo, S. J., Henderson, J. M., et al. (2016). A multiyear estimate of methane fluxes in Alaska from CARVE atmospheric observations. *Global Biogeochemical Cycles*, *30*(10), 1441–1453. https://doi.org/10.1002/2016GB005419

Minsley, B. J., Pastick, N. J., Wylie, B. K., Brown, D. R. N., & Kass, M. A. (2016). Journal of Geophysical Research: Earth Surface after fire in boreal landscapes. *Journal of Geophysical Research: Earth Surface*, *121*, 320–335. https://doi.org/10.1002/2015JF003781

Minsley, B. J., Wellman, T. P., Walvoord, M. A., & Revil, A. (2015). Sensitivity of airborne geophysical data to sublacustrine and near-surface permafrost thaw. *The Cryosphere*, *9*(2), 781–794. https://doi.org/10.5194/tc-9-781-2015

Morel, X., Decharme, B., Delire, C., Krinner, G., Lund, M., Hansen, B. U., & Mastepanov, M. (2019). A new process-based soil methane scheme: Evaluation over arctic field sites with the ISBA land surface model. *Journal of Advances in Modeling Earth Systems*, *11*(1), 293–326. https://doi.org/10.1029/2018MS001329

Myhre, G., Shindell, D., Bréon, F.-M., Collins, W., Fuglestvedt, J., Huang, J., et al. (2013). Anthropogenic and natural radiative forcing. In T. F. Stocker, D. Qin, G.-K. Plattner, M. Tignor, S. K. Allen, J. Boschung, et al. (Eds.), *Climate change 2013: The physical science basis. Contribution of Working Group I to the Fifth Assessment Report of the Intergovernmental Panel on Climate Change* (pp. 659–740). Cambridge University Press.

Nahlik, A. M., & Mitsch, W. J. (2011). Methane emissions from tropical freshwater wetlands located in different climatic zones of Costa Rica. *Global Change Biology*, *17*(3), 1321–1334. https://doi.org/10.1111/j.1365-2486.2010.02190.x

Oberle, F. K. J., Gibbs, A. E., Richmond, B. M., Erikson, L. H., Waldrop, M. P., & Swarzenski, P. W. (2019). Towards determining spatial methane distribution on Arctic permafrost bluffs with an unmanned aerial system. *SN Applied Sciences*, *1*(3). https://doi.org/10.1007/s42452-019-0242-9

Olefeldt, D., Goswami, S., Grosse, G., Hayes, D., Hugelius, G., Kuhry, P., et al. (2016). Circumpolar distribution and carbon storage of thermokarst landscapes. *Nature Communications*, *7*, 13043. https://doi.org/10.1038/ncomms13043

Olefeldt, D., Turetsky, M. R., Crill, P. M., & McGuire, A. D. (2013). Environmental and physical controls on northern terrestrial methane emissions across permafrost zones. *Global Change Biology*, *19*(2), 589–603. https://doi.org/10.1111/gcb.12071

Peltola, O., Vesala, T., Gao, Y., Räty, O., Alekseychik, P., Aurela, M., et al. (2019). Monthly gridded data product of northern wetland methane emissions based on upscaling eddy covariance observations. *Earth System Science Data Discussions*, *11*(3), 1263–1289. https://doi.org/10.5194/essd-11-1263-2019

Roberts, D. A., Gardner, M., Church, R., Ustin, S., Scheer, G., & Green, R. O. (1998). Mapping chaparral in the Santa Monica Mountains using multiple endmember spectral mixture models. *Remote Sensing of Environment*, *65*(3), 267–279. https://doi.org/10.1016/s0034-4257(98)00037-6

Schuur, E. A. G., McGuire, A. D., Schädel, C., Grosse, G., Harden, J. W., Hayes, D. J., et al. (2015). Climate change and the permafrost carbon feedback. *Nature*, *520*(7546), 171–179. https://doi.org/10.1038/nature14338

Sepulveda-Jauregui, A., Walter Anthony, K. M., Martinez-Cruz, K., Greene, S., & Thalasso, F. (2015). Methane and carbon dioxide emissions from 40 lakes along a north–south latitudinal transect in Alaska. *Biogeosciences*, *12*(11), 3197–3223. https://doi.org/10.5194/bg-12-3197-2015

Serikova, S., Pokrovsky, O. S., Laudon, H., Krickov, I. V., Lim, A. G., Manasypov, R. M., & Karlsson, J. (2019). High carbon emissions from thermokarst lakes of Western Siberia. *Nature Communications*, *10*(1), 1–7. https://doi.org/10.1038/s41467-019-09592-1

Ström, L., Ekberg, A., Mastepanov, M., & Christensen, T. R. (2003). The effect of vascular plants on carbon turnover and methane emissions from a tundra wetland. *Global Change Biology*, *9*(8), 1185–1192. https://doi.org/10.1046/j.1365-2486.2003.00655.x

Sturtevant, C. S., & Oechel, W. C. (2013). Spatial variation in landscape-level $CO_2$ and $CH_4$ fluxes from arctic coastal tundra: Influence from vegetation, wetness, and the thaw lake cycle. *Global Change Biology*, *19*(9), 2853–2866. https://doi.org/10.1111/gcb.12247

Sweeney, C., Chatterjee, A., Wolter, S., Mckain, K., Bogue, R., Newberger, T., et al. (2020). Atmospheric carbon cycle dynamics over the ABoVE domain: An integrated analysis using aircraft observations (Arctic-CAP) and model simulations (GEOS). *Atmospheric Chemistry and Physics Discussions*, 1–30. https://doi.org/10.5194/acp-2020-609

Sweeney, C., Dlugokencky, E., Miller, C. E., Wofsy, S., Karion, A., Dinardo, S., et al. (2016). No significant increase in long-term $CH_4$ emissions on North Slope of Alaska despite significant increase in air temperature. *Geophysical Research Letters*, *43*, 1–8. https://doi.org/10.1002/2016GL069292

Thompson, D. R., Leifer, I., Bovensmann, H., Eastwood, M., Fladeland, M., Frankenberg, C., et al. (2015). Real-time remote detection and measurement for airborne imaging spectroscopy: A case study with methane. *Atmospheric Measurement Techniques*, *8*(10), 4383–4397. https://doi.org/10.5194/amt-8-4383-2015

Thornton, B. F., Prytherch, J., Andersson, K., Brooks, I. M., Salisbury, D., Tjernström, M., & Crill, P. M. (2020). Shipborne eddy covariance observations of methane fluxes constrain Arctic sea emissions. *Science Advances*, *6*(5), 1–11. https://doi.org/10.1126/sciadv.aay7934

Thornton, B. F., Wik, M., & Crill, P. M. (2016). Double-counting challenges the accuracy of high-latitude methane inventories. *Geophysical Research Letters*, *43*(24), 12569–12577. https://doi.org/10.1002/2016GL071772

Thorpe, A. K., Duren, R. M., Conley, S., Prasad, K. R., Bue, B. D., Yadav, V., et al. (2020). Methane emissions from underground gas storage in California. *Environmental Research Letters*, *15*(4), 045005. https://doi.org/10.1088/1748-9326/ab751d

Thorpe, A. K., Frankenberg, C., Aubrey, A. D., Roberts, D. A., Nottrott, A. A., Rahn, T. A., et al. (2016). Mapping methane concentrations from a controlled release experiment using the next generation airborne visible/infrared imaging spectrometer (AVIRIS-NG). *Remote Sensing of Environment*, *179*, 104–115. https://doi.org/10.1016/j.rse.2016.03.032

Thorpe, A. K., Frankenberg, C., & Roberts, D. A. (2014). Retrieval techniques for airborne imaging of methane concentrations using high spatial and moderate spectral resolution: Application to AVIRIS. *Atmospheric Measurement Techniques*, *7*(2), 491–506. https://doi.org/10.5194/amt-7-491-2014

Thorpe, A. K., Roberts, D. A., Bradley, E. S., Funk, C. C., Dennison, P. E., & Leifer, I. (2013). High resolution mapping of methane emissions from marine and terrestrial sources using a Cluster-Tuned Matched Filter technique and imaging spectrometry. *Remote Sensing of Environment*, *134*, 305–318. https://doi.org/10.1016/j.rse.2013.03.018

Torre Jorgenson, M., Harden, J., Kanevskiy, M., O'Donnell, J., Wickland, K., Ewing, S., et al. (2013). Reorganization of vegetation, hydrology and soil carbon after permafrost degradation across heterogeneous boreal landscapes. *Environmental Research Letters*, *8*(3), 035017. https://doi.org/10.1088/1748-9326/8/3/035017

Treat, C. C., Marushchak, M. E., Voigt, C., Zhang, Y., Tan, Z., Zhuang, Q., et al. (2018). Tundra landscape heterogeneity, not inter-annual variability, controls the decadal regional carbon balance in the Western Russian Arctic. *Global Change Biology*, 1–17. https://doi.org/10.1111/gcb.14421

Turetsky, M. R., Abbott, B. W., Jones, M. C., Anthony, K. W., Olefeldt, D., Schuur, E. A. G., et al. (2020). Carbon release through abrupt permafrost thaw. *Nature Geoscience*, *13*(2), 138–143. https://doi.org/10.1038/s41561-019-0526-0

Walter Anthony, K., Daanen, R., Anthony, P., Schneider Von Deimling, T., Ping, C.-L., Chanton, J. P., & Grosse, G. (2016). Methane emissions proportional to permafrost carbon thawed in Arctic lakes since the 1950s. *Nature Geoscience*, *9*(9), 679–682. https://doi.org/10.1038/ngeo2795

Walter Anthony, K. M., & Anthony, P. (2013). Constraining spatial variability of methane ebullition seeps in thermokarst lakes using point process models. *Journal of Geophysical Research: Biogeosciences*, *118*, 1015–1034. https://doi.org/10.1002/jgrg.20087

Walter Anthony, K. M., Anthony, P., Grosse, G., & Chanton, J. (2012). Geologic methane seeps along boundaries of Arctic permafrost thaw and melting glaciers. *Nature Geoscience*, *5*(6), 419–426. https://doi.org/10.1038/ngeo1480

Walter Anthony, K. M., Schneider von Deimling, T., Nitze, I., Frolking, S., Emond, A., Daanen, R., et al. (2018). 21st-century modeled permafrost carbon emissions accelerated by abrupt thaw beneath lakes. *Nature Communications*, *9*(1), 3262. https://doi.org/10.1038/s41467-018-05738-9

Walter Anthony, K. M., Vas, D. A., Brosius, L., Chapin, F., III, Zimov, S., & Zhuang, Q. (2010). Estimating methane emissions from northern lakes using ice-bubble surveys. *Limnology and Oceanography: Methods*, *8*, 592–609. https://doi.org/10.4319/lom.2010.8.0592

Walter, K. M., Chanton, J. P., Chapin, F. S., Schuur, E. A. G., & Zimov, S. A. (2008). Methane production and bubble emissions from arctic lakes: Isotopic implications for source pathways and ages. *Journal of Geophysical Research*, *113*, G00A08. https://doi.org/10.1029/2007JG000569

Wickland, K. P., Striegl, R. G., Neff, J. C., & Sachs, T. (2006). Effects of permafrost melting on $CO_2$ and $CH_4$ exchange of a poorly drained black spruce lowland. *Journal of Geophysical Research*, *111*(2), 1–13. https://doi.org/10.1029/2005JG000099

Windsor, J., Moore, T. R., & Roulet, N. T. (1992). Episodic fluxes of methane from subarctic fens. *Canadian Journal of Soil Science*, *72*(4), 441–452. https://doi.org/10.4141/cjss92-037

Zona, D., Gioli, B., Commane, R., Lindaas, J., Wofsy, S. C., Miller, C. E., et al. (2015). Cold season emissions dominate the Arctic tundra methane budget. *Proceedings of the National Academy of Sciences of the United States of America*, *113*(1), 40–45. https://doi.org/10.1073/pnas.1516017113

## References From the Supporting Information

Hanna, S. R., Briggs, G. A., & Hosker, R. P., Jr. (1982). *Handbook on atmospheric diffusion* (Research Report No. DOE/TIC-11223). National Oceanic and Atmospheric Administration and Atmospheric Turbulence and Diffusion Laboratory.

Theiler, J. (2012). The incredible shrinking covariance estimator. In *Automatic target recognition XXII* (Vol. 8391, p. 83910P). International Society for Optics and Photonics.

Thompson, D. R., Thorpe, A. K., Frankenberg, C., Green, R. O., Duren, R., Guanter, L., et al. (2016). Space-based remote imaging spectroscopy of the Aliso Canyon CH4 superemitter. *Geophysical Research Letters*, *43*(12), 6571–6578.